Parametric analysis, response surface, sensitivity analysis, and optimization of a novel spiral-double ground heat exchanger

Ahmed A. Serageldin[1,2], Ali Radwan[1,3], Takao Katsura[1], Yoshitaka Sakata[1], Shigeyuki Nagasaka[4] and Katsunori Nagano[1]

[1]Division of Human Environmental Systems, Faculty of Engineering, Hokkaido University, N13-W8, Kita-ku, Sapporo 060-8628, Japan

[2]Mechanical Power Engineering Department, Faculty of Engineering at Shoubra, Benha University, Shoubra 11629, Egypt

[3]Mechanical Power Engineering Department, Faculty of Engineering, Mansoura University, El Mansoura 35516, Egypt

[4]Shin Nippon Kucho CO., Ltd., Yokohama, Tokyo, Japan

Highlights

1. **A novel spiral-double ground heat exchanger design is proposed.**
2. **A numerical comparison between the single U-tube, spiral, and spiral-double GHX was carried out.**
3. **Parametric, sensitivity, and response surface analyses were conducted.**
4. **The MOGA optimization method was applied.**
5. **Three optimum candidates were introduced.**

Abstract

This paper proposes a novel spiral-double ground heat exchanger (GHX) that decreases conventional construction costs, facilitates installation, promotes heat transfer, and reduces thermal resistance. In this study, a new and effective installation procedure was proposed. Three-dimensional, transient, and conjugated finite volume simulations were conducted to compare the thermo-hydraulic performance of the traditional single U-tube and spiral GHXs with the proposed spiral-double GHX under two different flow rates. Moreover, a parametric analysis was conducted to study the impact of the design, operating, and geological parameters on the thermal performance of the new spiral-double GHX. Finally, surface response and sensitivity analyses, as well as optimization, were carried out using the ANSYS workbench. The comparison revealed that the spiral-double GHX yields higher thermal effectiveness (E) and heat transfer rate (Q) than single-U tubes GHX by 40.8 % and 44.1 %, respectively. In addition, it has a lower thermal resistance of 75.3 % than the single-U tube GHX under turbulent flow conditions. Furthermore, the parametric study and sensitivity analysis concluded that the spiral radius has the most significant impact, followed by flow velocity, tube diameter, and pitch distance. Moreover, the recommended fluid velocity does not exceed 0.21 m/s, pitch distance of 0.0625 m, a spiral radius of 0.2 m, and grout conductivity of 2.1 W/m.K.

Keywords: Ground source heat pump; Spiral-double ground heat exchanger; Parametric analysis; Sensitivity analysis; Numerical optimization

Nomenclature

List of symbols	
a	The soil thermal diffusivity [m^2/s]
C_p	Specific heat at constant pressure [J/kg·K]
C_μ, σ_ε, σ_k, $C_{1\varepsilon}$, and $C_{2\varepsilon}$	The empirical constants [-]
D_i	Pipe inner diameter [m]
D_o	Pipe outer diameter [m]
E	Thermal effectiveness [-]
H	Ground heat exchanger depth [m]
$\vec{F}$	The external body force [N/m^3]
K	Thermal conductivity [W/m·K]
P	Ground heat exchanger pitch [m]
P_e	Pump electrical power [W]
q	The bsorbed heat flux [W/m^2]
Rb	Borehole heat exchanger thermal resistance [m·K/W]
r_b	The borehole radius [m]
S_k, S_ε	The source terms of *k*-equation and ε equation [-]
T_0	The undisturbed ground temperature [K]
T_f	The average fluid temperature [ºC]
Q	The injected heat power in [kW]
k	The turbulent kinetic energy per unit mass [J/kg]
p	The static pressure [N/m^2]
Greek symbol	
$\dot{V}$	Fluid volume flow rate [m^3/s]
η_{pump}	The overall pump efficiency [-]
$\vec{v}$	The velocity vector [m/s]
$\bar{\bar{\tau}}$	The surface shear stress [N/m^2]
$\nabla \cdot (k_f \nabla T_f)$	The diffusive heat transfer term [W]
Ks	The soil thermal conductivity [W/m·K]

ε	The rate of dissipation of turbulent kinetic energy per unit mass [m^2/s^3]
μ	The dynamic viscosity [m^2/s]
ρ	Material Density [kg/m^3]
σ_k and σ_ε	The Prandtl numbers of k and ε equations [-]
Φ_{pi}	borehole inner diameter [m]
Φ_s	Soil domain diameter [m]
γ	The Euler constant
$\rho\vec{g}$	The gravitational body force [N/m^3]
τ	The time from the beginning of heating [sec]
Abbreviations	
3-D	Three-dimensional
CFD	Computational fluid dynamic
GB	Giga Byte
GHX	Ground heat exchanger
GSHP	Ground source heat pump
HDPE	High-density polyethylene
PE	Polyethylene
PVC	Polyvinyl chloride
SIMPLE	The Semi-Implicit method algorithm
TPC	Thermal performance capability
TRT	Thermal response test
UDF	User defined function
UTB	Underground thermal Battery
Subscripts	
eff	Effective
f	Fluid
In, out	Inlet and outlet
l	Borehole depth
net	Net heat exchange
b	Borehole

1. Introduction

The use of the ground as a heat source or heat sink in ground source heat pump (GSHP) systems has attracted significant attention from the research community for space heating and cooling, respectively [1], owing to their high energy efficiency and low environmental impact [2]. Many recent numerical and experimental investigations have been conducted to design and propose new ground heat exchangers (GHXs) for GSHP systems. GHXs are used to dissipate or absorb heat from the ground and can be horizontally [3] or vertically [4,5]installed. In the vertical design, GHXs are buried at depths from 15 to 150 m, while the horizontal GHX is buried in trenches from 1 to 2 m deep [6]. GHXs can also be applied to the pile foundations of buildings to reduce installation costs [7]. The GHX can be placed under the building foundation in the base ground layer or the building foundation concrete layer [8].

Several investigations have been conducted to examine the effect of tube shape [5], heat carrier type [9], GHX depths [10,11], and tube materials [12,13]. Di Qi et al. [14] studied the impact of GHX connection configurations on ground temperature and GSHP performance. They used a numerical simulation developed by ANSYS Fluent software to study the effect of using parallel and series connections of multiple U-tube GHX and concluded that connecting multiple U-tube GHXs in a parallel configuration attained a higher heating performance. In addition, the pressure drop across the multiple connected U-tube GHX with a series configuration was higher than that of the parallel configuration. Congedo et al. [15] investigated the effect of different burial depths and various ground thermal conductivities on the thermal performance of a horizontal air GHX. They concluded that the ground thermal conductivity slightly affected the thermal performance of the horizontal air GHX. Li et al. [4] investigated the use of a deep-buried coaxial double-pipe GHX in a GSHP system. They concluded that the buried pipe system's heat extraction capacity could be enhanced by changing the shape of the inner pipe. Warner et al. [16] proposed a novel GHX design called an underground thermal battery (UTB) and concluded that the proposed UTB has similar performance and lower cost than conventional GHX.

Among these designs, the spiral tube GHX has been commonly studied in recent years, where a spiral pipe is fitted into the pile of the building foundation or in the borehole. The inlet water enters from the spiral tube of the GHX, and water is allowed to exit from the straight center tube [6]. Jalaluddin and Miyara [6] numerically compared the thermal and hydraulic analyses of a spiral GHX with a conventional U-tube GHX. They investigated the effect of changing the helical coil pitch on the heat exchange rate and pressure drop. Different spiral GHXs with pitches of 0.05, 0.1, and 0.2 m were investigated. Two water flow rate conditions of 2 L/min and 8 L/min were used to estimate the GHX performance under laminar and turbulent conditions, respectively. After comparison with the straight U-tube GHX, they concluded that using the spiral GHX in the borehole augmented the heat exchange rate, and this increment was more pronounced at a smaller helical pitch of 0.05. However, the water pressure drop also increased because of the increase in the tube length and spiral geometry. Zarrella et al. [17] conducted a comparative heat transfer analysis of a helical and triple U-tube GHX installed inside a foundation pile. They concluded that the helical pipe GHX provides a higher thermal performance than the triple U-tube GHX. In addition, the helical tube pitch significantly affects the peak load.

Blázquez et al. [18] experimentally analyzed the thermal performance of a single or double U-tube GHX with and without longitudinal spacers compared to a helical-shaped pipe GHX. Small-scale vertical closed-loop GHX experiments were performed. They claimed that the spiral GHX offered a lower required drilling depth compared to the U-tube configuration. This results in significant economic savings during drilling. Zarrella et al. [19] performed a detailed numerical study to compare the performance of a conventional double U-tube and a helical-tube GHX for GHSP systems. They analyzed the heat transfer attributes of these two types of GHX using the thermal resistance and capacitance approach via long- and short-term simulations. Saeidi et al. [20] numerically investigated using spatial aluminum rods with a shallow depth spiral GHX. The rods firmly hold the pipe inside the borehole and improves the heat transfer rate by 31 %. Simultaneously, the spiral GHX was more efficient than these two shapes in terms of long-term and short-term thermal loads, as claimed by Zhao et al. [21]. Javadi et al. [22,23] proposed a new GHX configuration, as shown in **Fig. 1**. They compared the results of the thermal performance coefficient (*TPC*) and thermal effectiveness (*E*). The results showed that the triple-helix GHX exhibited the best performance compared to other GHXs.

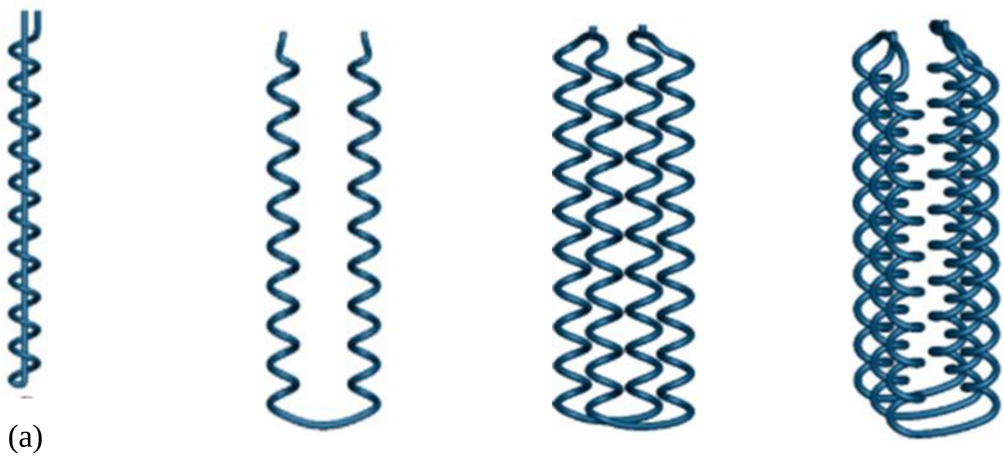

(a)

(b) (c) (d)

Fig. 1. Schematic of GHX configurations used in [22] (a) Helix (inner outlet), (b) Helix (U-tube), (c) Double helix, and (d) Trible helix GHXs

Although the former researchers dedicated their studies to enhance the thermal performance of the GHX, their novel designs had missed the practical suitability and overall performance analysis. Therefore the present study focused mainly on proposing a new spiral-double GHX and clarify its practical advantages and overall performance superiority compared with the customary single-U-tube and helical GHX. In this paper, section 2 explains the new installation procedure of the proposed GHX to decrease the damage risk and save installation cost and time. Section 3 demonstrates the numerical simulation set-up procedure, and section 4 describes the analysis methodology and how the overall performance indexes are calculated. Section 5 discloses the parametric analysis, surface response, and optimization processes to find the optimum design parameters and operating conditions of such new GHX. Finally, section 6 quantitatively and qualitatively interprets and discusses the numerical results and optimization.

2. New GHX design and installation procedure

The new GHX is composed of two helical tubes connected at the ends, but it is different from the design proposed by Javadi et al. [19], shown in **Fig. 1.** Our design has the advantage that both helical tubes are intertwined in the form of plexus, which becomes more compact and concise. Moreover, the plexus is more flexible to be folded to the minimum size, giving easy transportation and handling. Simultaneously, it can be elongated in a flexible way to fit with the entire length of the borehole or piles, as shown in **Fig.2.** The pitch distance is kept with the help of the two sides' strips. The helical form enhances the heat exchange between the heat carrier and the surroundings by the impact of the secondary flow generated from the centrifugal force caused by the turns and curves of the helical path. Consequently, the heat exchange rate can be enlarged for the same borehole depth compared with the customary single-U tube and helical GHX. According to these advantages, the new spiral-double GHX can fit easily inside tight boreholes and becomes more suitable for densely urban areas, more energy-efficient, and lower installation and construction costs.

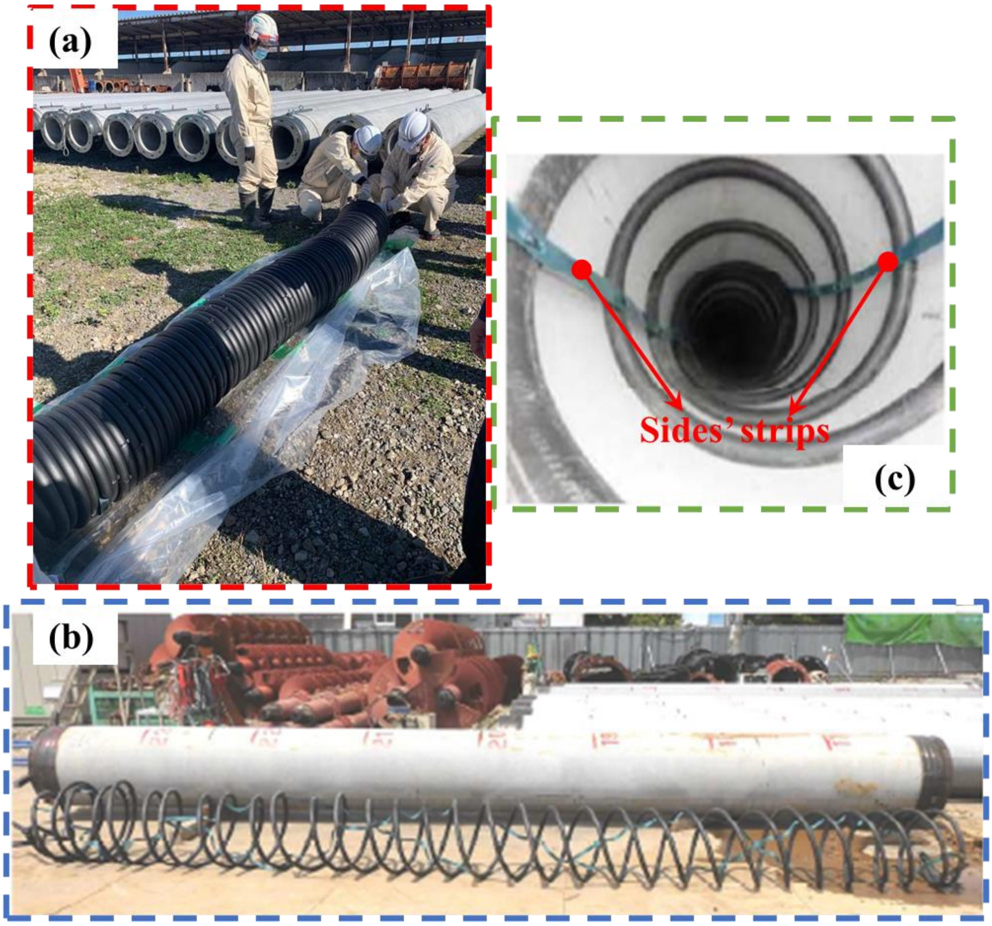

Fig. 2 The new spiral-double GHX (a) Folded form, (b) elongated form, and (c) the supporting sides' strips

As revealed by a previous literature survey and a comprehensive literature review conducted by Javadi et al. [24], most studies confirmed the performance privilege of helical GHX compared with a customary U-tube. However, the literature did not compare or estimate the practical difficulties in the installation procedure of helical GHX. The following steps and **Fig. 3.** detail the challenges of installing a helical GHX inside a borehole or energy pile, as summarized by Laloui et al. [25].

a- A large number of pipes are required for energy harvesting.

b- A large number of fittings and connections are required to connect multiple tubes loops.

c- Pipe bending or thermally welded U-bends are used at the edge of the borehole.

d- A reinforced structural support cage is required to fix the pipes, which is constructed on-site, before placing the cage inside the borehole.

e- There is a high possibility of loop damage during installation.

(a) (b) (c)

Fig. 3. Installation procedure and difficulties of GHX (a) Thermally welded U-bend, (b) Pipe bending at the end edge of the GHX, and (c) Multi-U tubes fixed by a steel cage

Therefore, the novelty of the present study is the proposal of a novel spiral-double GHX that facilitates the installation procedure with a lower damage risk and mitigates the need for the steel cage, as shown in **Fig. 4**. The following steps summarize the proposed installation procedure: a) compressing the spiral-double heat exchanger to be folded with a length of 2.6 m through the sidebars, b) attach the upper and bottom fixtures, c) attach the weight to the bottom part of the GHX, d) lift the folded spiral-double GHX using a crane hook, e) place the GHX inside the borehole, and f) expand and fix the GHX at the top of the borehole and collect the tube from the borehole head.

Using this novel spiral-double GHX, there is no need for elbows, fittings, and steel cages. In addition, this technique decreases the time required for installation and the required workforce while reducing the risk of damage.

The next step is to evaluate the thermo-hydraulic performance of the spiral-double GHX and compare it with the performance of the helical GHX. The two heat exchangers have the same tube diameter, borehole diameter, and depth and spiral pitch.

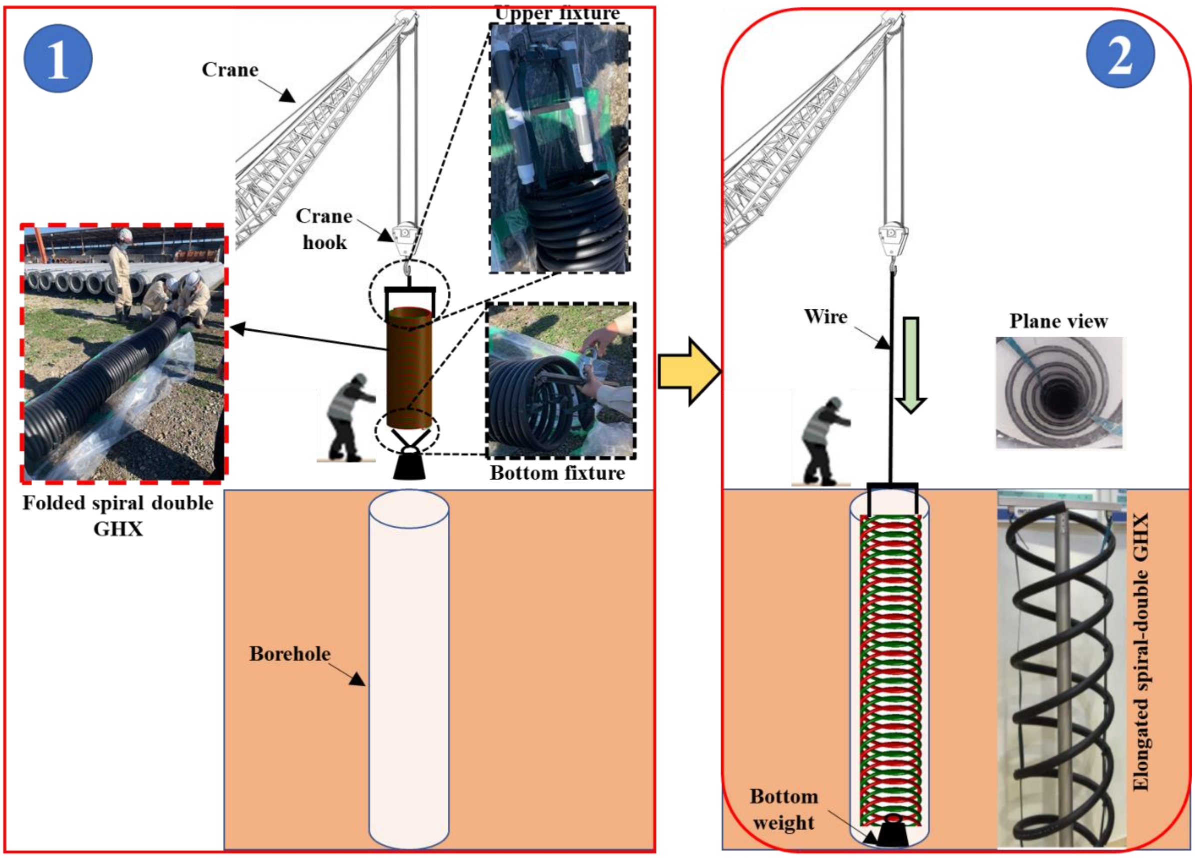

Fig. 4. Proposed installation procedure of the new spiral-double GHX

Therefore, a three-dimensional, transient numerical model was developed to calculate the flowing fluid temperature (T_{out}), borehole outer wall temperature (T_{p}), heat flux absorbed at the outer borehole wall (q_{p}), borehole thermal resistance (R_b), thermal effectiveness (E), pressure drop (ΔP), thermal performance capability (TPC), net heat gain (Q_{net}), and COP improvement. Then, a parametric study was conducted to explore the effects of pipe diameter (d_{p}), spiral diameter (D_b), grout material, fluid flow rate ($\dot{V}$), and coil pitch (P) on spiral-double GHX's thermal performance. Finally, response surface, sensitivity analysis, analyses, and optimization were carried out using the Design Explorer tools available in the ANSYS workbench, as summarized in **Fig. 5**.

3. Model development

The conjugated heat and fluid flow through the heat exchanger and the surrounding grouting and soil materials were solved simultaneously using an iterative approach based on a computational fluid dynamics (CFD) simulation. The CFD simulations relied on the finite volume approach via the ANSYS FLUENT environment in which heat is transferred by convection from the fluid to the heat exchanger's inner surface and then by conduction through the pipe material, grouting material, and soil. The study conducted by Jalaluddin et al. [6] was used to validate the CFD simulation of a spiral GHX. The spiral heat exchanger was constructed using high-density polyethylene tubes with inner and outer diameters of 26 mm and 33 mm, respectively, and a pitch of 20 mm, with a spiral diameter of 139.8 mm. The heat exchanger depth was 20 m, and the borehole was filled with the silica sand grouting material. The soil domain surrounding the borehole has a radius of 5 m and consists of clay to a depth of 15 m, below that of sandy clay. **Table 1** lists the thermophysical properties of the materials used in this study.

The following assumptions were used to simplify and accelerate solution identification:

1- The thermo-physical properties of materials are temperature independent.
2- Soil properties are considered homogeneous in all domains.
3- The convection and advection heat transfer owing to the impact of groundwater flow were neglected.
4- The flowing fluid is water and considered as an incompressible fluid.
5- The radiation, convection, and evaporation heat losses from the ground surface were neglected.

Table 1 Thermophysical properties of materials used in this study

	ρ [kg/m^3]	C_p [J/kg·K]	K [W/m·K]
Soil (depth <15 m)	1700	1800	1.2
Soil (depth >15 m)	1960	1200	2.1
Grout	2210	750	1.4
Pipe	920	2300	0.35

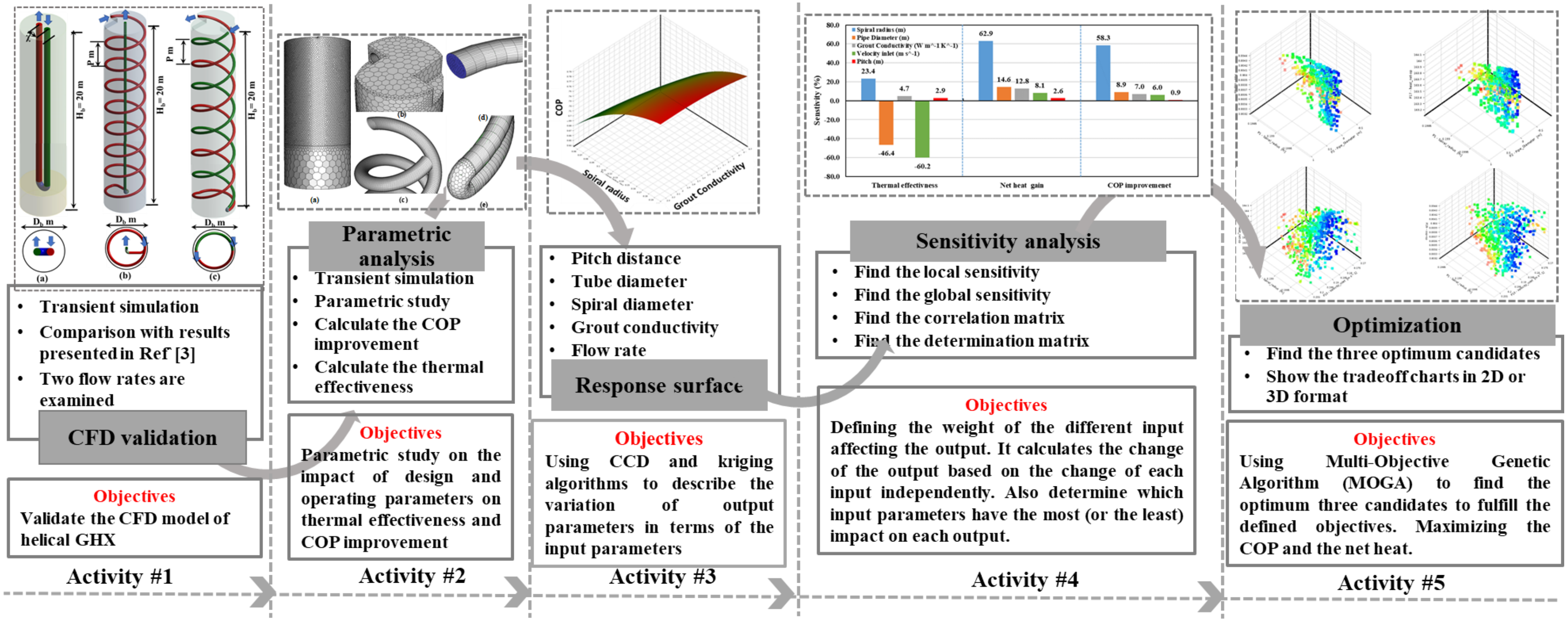

Fig. 5. Workflow diagram

The conservation equations of mass, momentum, and energy in three-dimensional and unsteady state forms are solved iteratively until convergence is achieved. The convergence criteria are predetermined to the limits of 10^{-3} for all equations, except at 10^{-6} for the energy equation. The continuity, momentum, and energy equations are solved for each cell face in the fluid domain inside the heat exchanger, as shown in **Eqs. 1, 2, 3, and 4** [26].

$$\frac{\partial \rho}{\partial t} + \nabla \cdot (\rho \vec{v}) = 0 \qquad (1)$$

Here, ρ is the fluid density in kg/m^3, and $\vec{v}$ is the velocity vector in m/s.

$$\frac{\partial}{\partial t}(\rho \vec{v}) + \nabla \cdot (\rho \vec{v} \vec{v}) = -\nabla p + \nabla \cdot (\bar{\bar{\tau}}) + \rho \vec{g} + \vec{F} \qquad (2)$$

Here, p is the static pressure in N/m^2, $\bar{\bar{\tau}}$ is the surface shear stress in N/m^2, $\rho \vec{g}$ is the gravitational body force in N/m^3, and $\vec{F}$, which is neglected in this study, is the external body force in N/m^3.

The convective conductive heat transfer in the fluid is described by **Eq. (4).**

$$\frac{\partial (\rho T_f)}{\partial t} + \nabla \cdot (\rho \vec{v} T_f) = \nabla \cdot \left(k_f \nabla T_f\right) + s \qquad (4)$$

Here, $\frac{\partial (\rho T_f)}{\partial t}$ is the rate of change of fluid temperature, $\nabla \cdot \left(\rho \vec{v} T_f\right)$ is the convective heat transfer term, $\nabla \cdot \left(k_f \nabla T_f\right)$ is the diffusive heat transfer term, and s is the energy source term, which was neglected in this study.

The energy conservation equation used for heat conduction within the solid domain was calculated using **Eq. (5).**

The realizable $\kappa - \epsilon$ is used to simulate the turbulent fluctuation of energy dissipation inside the boundary layer near the tube wall. It provides superior performance for flows involving boundary layers under strong adverse pressure gradients, separation, and recirculation. It also offers accurate and fast convergence for high-Reynolds number applications [27].

The κ *and* ϵ equations for $\kappa - \epsilon$ turbulence model are written as follows.

$$\frac{\partial (\rho k)}{\partial t} + \mathrm{div}(\rho k \vec{v}) = \mathrm{div}\left[\frac{\mu_t}{\sigma_k} \mathrm{grad} k\right] + \mu_t G + S_k - \rho \varepsilon \qquad (6)$$

$$\frac{\partial (\rho \varepsilon)}{\partial t} + \mathrm{div}(\rho \varepsilon \vec{v}) = \mathrm{div}\left[\frac{\mu_t}{\sigma_k} \mathrm{grad} \varepsilon\right] + C_{1\varepsilon} \frac{\varepsilon}{K} \mu_t G + S_\varepsilon - C_{2\varepsilon} \rho \frac{\varepsilon^2}{K} \qquad (7)$$

where k is the turbulent kinetic energy per unit mass (m^2/s^2); ε is the rate of dissipation of turbulent kinetic energy per unit mass (m^2/s^3); S_k and S_ε are the source terms (kg/m·s^3); σ_k and σ_ε are the Prandtl numbers of k and ε, respectively; μ_t is the eddy viscosity (kg/m·s); G is the turbulent production rate

(1/s^2); v is the fluid velocity vector; and C_μ, σ_ε, σ_k, $C_{1\varepsilon}$, and $C_{2\varepsilon}$ are empirical constants, where $C_\mu = 0.09$, $\sigma_\varepsilon = 1.2$, $\sigma_k = 1$, $C_{1\varepsilon} = 1.44$, and $C_{2\varepsilon} = 1.9$.

The enhanced wall treatment was used to predict the near-wall turbulence inside the turbulence boundary layer.

3.1. Boundary and operating conditions

Two flow rates were set for evaluation under laminar and turbulent flow conditions. The laminar flow condition occurred at a flow rate of 2 L/min, while turbulent flow was achieved at a flow rate of 8 L/min. The upper and lower walls were considered to be isothermal conditions.

The geometry and dimensions are illustrated in **Fig. 6** and listed in **Table 2.** Moreover, the boundary conditions indicated in **Fig. 6** and listed in **Table 3.**

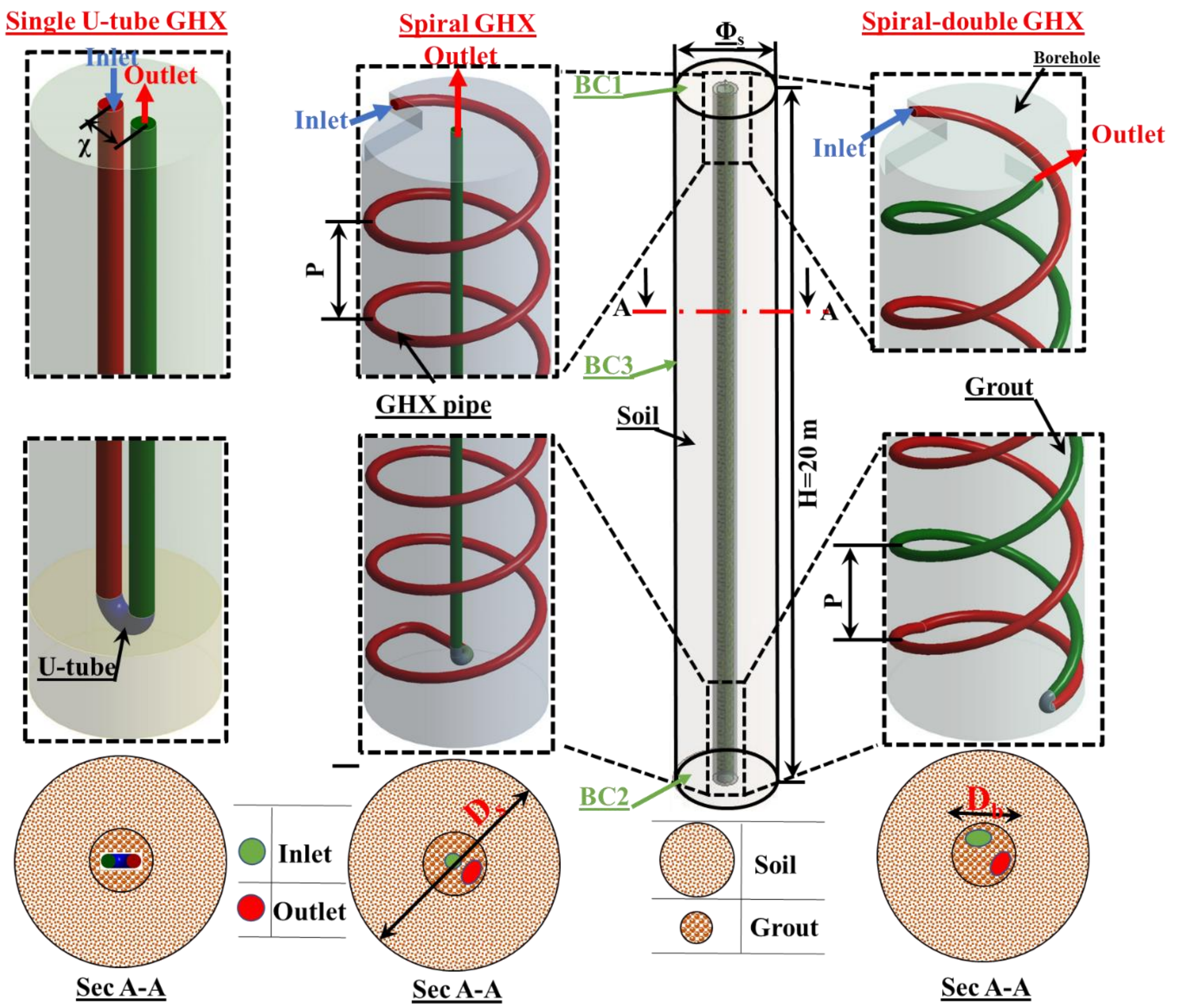

Fig. 6. Geometry, dimensions, and boundary conditions used in this study

Table 2 Geometry dimensions

Soil domain diameter, Φ_s	10 m
GHX depth, H	20 m
GHX pitch, P	0.2 m
GHX pipe inner diameter, D_i	0.026 m
GHX pipe inner diameter, Do	0.033 m

Table 3 Boundary conditions

Boundary	Flow rate	Velocity	Pressure	Temperature/Heat flux
Inlet	2 L/min	0.063 m/s	-	27 ^oC
	8 L/min	0.25 m/s		
Outlet	-	-	0 Pa	-
BC1		-	-	Adiabatic
BC2		-	-	17.7 ^oC
BC3		-	-	17.7 (y)

Moreover, the thermal response comparison between the spiral and spiral-double GHX was carried out under an unsteady state.

a) The transient simulation includes predicting the fluid outlet temperature when the inlet temperature is 27 °C under laminar and turbulent flow conditions, and the heat transfer rate from the GHX to the surrounding soil was calculated.

b) A parametric study was conducted to investigate the impact of the pipe diameter (d_p), spiral diameter (Φ_p), fluid flow rate ($\dot{V}$), grout material thermal conductivity (K_g), and pitch distance (P) on the thermal resistance and heat transfer attributes inside the grout and surrounding soil. Fourteen simulations were conducted under the conditions described in **Table 4.**

Table 4 Boundary conditions for parametric analysis

	Case	Flow rate L/min	Pitch m	Tube diameter m	Borehole diameter m	Spiral diameter m	Grout material W/m.K
Flow rate	1	2	0.10	0.026	0.18	0.1398	1.4
	2	8	0.10	0.026	0.18	0.1398	1.4
Pitch	3	8	0.05	0.026	0.18	0.1398	1.4
	4	8	0.15	0.026	0.18	0.1398	1.4
	5	8	0.20	0.026	0.18	0.1398	1.4
	6	8	0.10	0.020	0.18	0.1398	1.4

Pipe diameter	7	8	0.10	0.030	0.18	0.1398	1.4
Borehole diameter	8	8	0.10	0.026	0.24	0.2	1.4
	9	8	0.10	0.026	0.3	0.26	1.4
	10	8	0.10	0.026	0.36	0.32	1.4
grout material	11	8	0.10	0.026	0.18	0.1398	0.7
	12	8	0.10	0.026	0.18	0.1398	2.4

3.2. Discretizing domains and element types

Various mesh element types were used to discretize the spatial domains of grouting and soil materials, as shown in **Fig. 7**. A mixture of polyhedral and tetrahedral elements was applied, while the sweep method was used to discretize the fluid domain. A mesh independent solution was also carried out to select the mesh element size and numbers for a cost-effective simulation, as shown in **Fig. 8**. Furthermore, inflation layers were adopted on the inner tube surface to capture the turbulent energy exchange inside the turbulent boundary layer. Ten layers with a total thickness of 1.5 mm were inflated inside the spiral heat exchanger tube and U-tube bending parts.

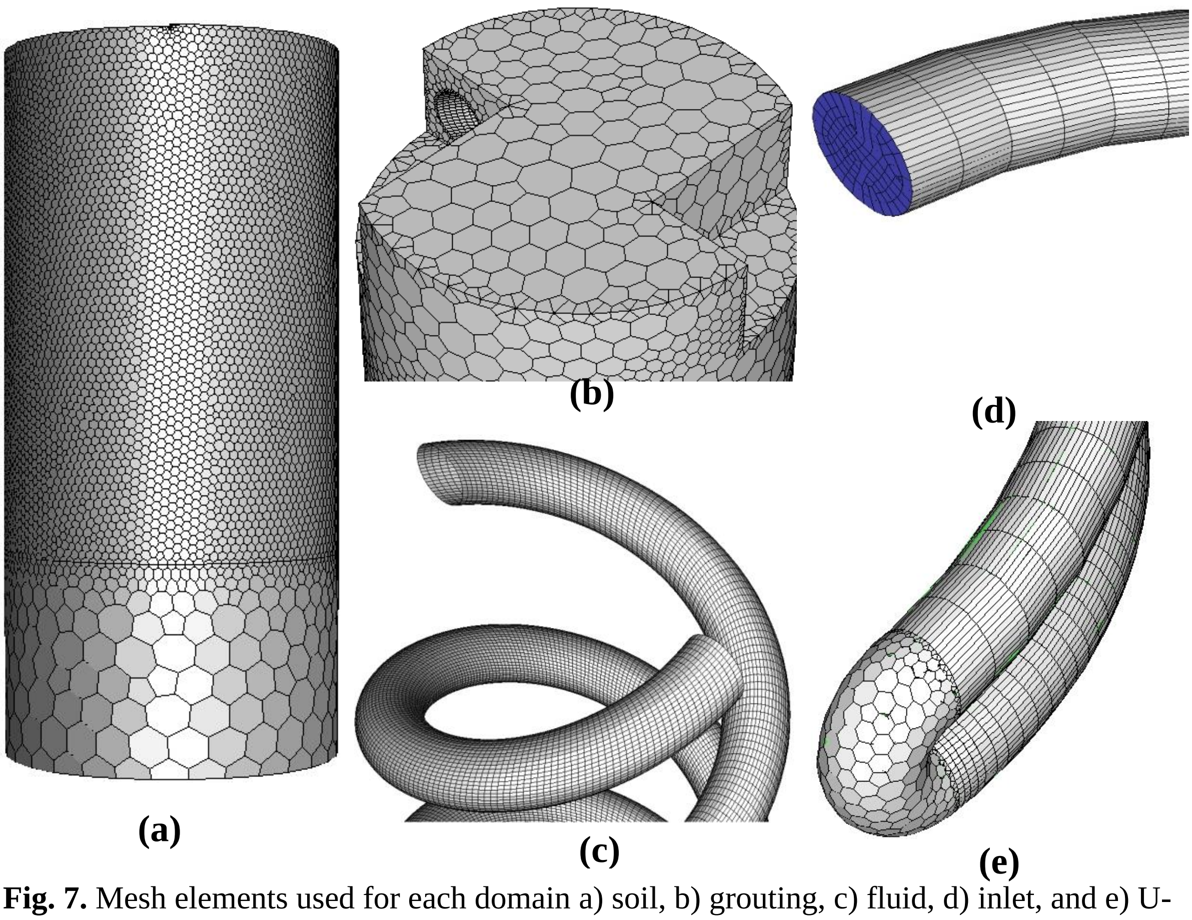

Fig. 7. Mesh elements used for each domain a) soil, b) grouting, c) fluid, d) inlet, and e) U-bend

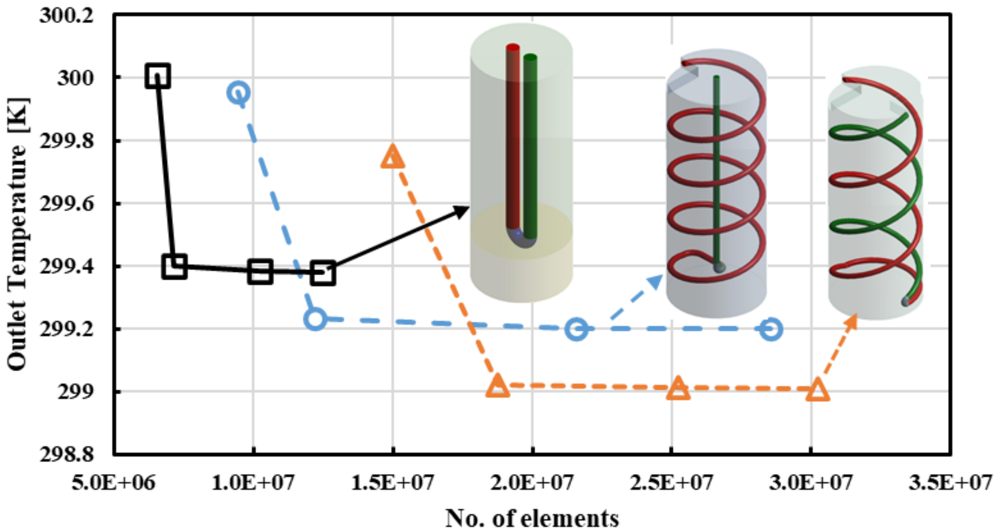

Fig. 8. Mesh independent solution test

3.3. Solver Schemes

In this study, the SIMPLE segregated algorithm was used to solve the pressure-velocity coupling inside the fluid domain. A second-order scheme was used to discretize the pressure, momentum, energy, turbulent kinetic energy (*K*-equation), and dissipation rate (ϵ-equation) equations. A first-order implicit scheme was used to formulate the transient behavior of the flowing fluid.

4. Analytic method

The numerical simulations predicted heat energy transfer by conduction to the surrounding soil and through the medium of the grout and the tube wall. Then, the thermal energy was conveyed by convection from the tube's inner surface to the flowing fluid. The fluid outlet temperature and borehole outer wall temperature were determined alongside the borehole surface's heat flux. These results were analyzed to calculate the following characteristics.

4.1. Total and net heat exchange rate ($\boldsymbol{Q}$, $\boldsymbol{Q_{net}}$)

In this study, the fluid outlet temperature (T_{out}) was predicted, and the average fluid temperature (T_f) was calculated. With the information of the fluid inlet, outlet temperatures along with the mass flow rate, fluid heat capacity, and heat exchange rate (Q) are calculated according to Eq. (9)

$$Q = \dot{m}C_p(T_{out} - T_{in}) \tag{9}$$

Furthermore, the pressure drop through the heat exchanger tube (ΔP) was predicted, and the pumping electrical power was calculated according to Eq. (10).

$$P_e = \Delta P \text{Q}/\eta_{pump}. \quad (10)$$

where P_e is the required pump electrical power (W), ΔP is the pressure drop through the tube (Pa), $\dot{V}$ is the fluid volume flow rate (m^3/s), and η_{pump} is the overall pump efficiency, including the hydraulic, mechanical, and motor efficiencies (0.42) [28].

The net utilized heat energy from the GHX is the difference between the thermal heat exchange rate and the thermal heat energy converted via the thermal power plant to the electricity required to derive the pump with a thermal efficiency (η_{th}) of 0.37[29], as indicated in Eq. (11).

$$Q_{net} = Q - \left(\frac{P_e}{\eta_{th}}\right). \quad (11)$$

4.2. Thermal effectiveness (*E*) and thermal resistance (*R_b*)

In addition, the borehole outer wall temperature (T_b) and heat energy rejected to the surrounding soil per unit depth (q_l) were predicted. Subsequently, the effective coefficient of the thermal energy (E) and thermal resistance (R_b) were determined.

E is the ratio between the actual and theoretical heat transfer capacities and indicates heat transfer efficiency, as explained by Eq. (12)[30]. Moreover, E is a dimensionless number that varies between zero and one, and it manifests the effectiveness of the GHX in delivering the maximum outlet temperature.

$$E = \frac{T_{out} - T_{in}}{T_g - T_{in}} \quad (12)$$

where T_{in} is the fluid inlet temperature (27 °C), and T_g is the undisturbed ground temperature (17.7 °C).

The total thermal resistance that impedes heat transfer through the pile, grout, and flowing fluid domains was calculated according to Eq. (13)[31].

$$R = \frac{\overline{T_f} - T_b}{q_b} \quad , \overline{Tf} = \frac{T_{in} + T_{out}}{2} \quad (13)$$

where $\overline{Tf}$ is the average value of the fluid inlet and outlet temperatures (in K), T_b is the average borehole wall temperature (in K), and q_p is the borehole wall heat flux per unit length (W/m) [32].

4.3. Thermal performance capability (*TPC*)

Furthermore, the pressure drop along the heat exchanger tube (ΔP) is the difference between the inlet and outlet pressures, which was predicted in the numerical simulation. The friction coefficient (f) was calculated using Eq. (14).

$$f = \frac{2d_h \Delta P}{\rho u^2 L_T} \quad (14)$$

where d_h is the hydraulic diameter of the tube (equal to d_i, m), ΔP is the pressure drop through the tube in Pa, ρ is the flowing fluid density in kg/m^3, u is the velocity of the fluid flowing through the tube in m/s, and L_T is the total pipe length in m, which is calculated by Eq. (15) for spiral GHX.

$$L_T = \frac{H}{P}\sqrt{(\pi D)^2 + P^2} \quad (15)$$

where H is the depth of the spiral GHX in m, P is the pitch of the spiral GHX in (m), and D is the diameter of the spiral GHX in (m).

Finally, the thermal performance capability (TPC) is a non-dimensional number that calculates the ratio between the normalized effectiveness and normalized friction, as shown in Eq. (16)[22].

$$TPC = \frac{E/E_0}{f/f_0}. \quad (16)$$

where E and E_0 are the effectiveness of the spiral GHX and single-U tube GHX, respectively, and f and f_0 are the friction coefficients of the spiral GHX and single-U tube GHX, respectively.

4.4. *COP* improvement

The net *COP* of the GSHP system depends mainly on the results of both the heat exchange rate and pumping power. The heat exchange rate indicates the useful output of the GSHP, while the input is the pumping power required to overcome the pressure drop that occurs inside the heat exchanger tube.

Therefore, a new criterion was proposed by Jalaluddin et al. [6] to calculate the improvement in the *COP*, as shown in Eq. (17), compared with the conventional single U-tube.

$$COP_{improvement} = \frac{Q'_H}{Q_H} - \frac{V\Delta P}{Q_H}\frac{\Delta P'}{\Delta P} > 0, \quad (17)$$

Where $COP_{improvement}$ is the improvement in the *COP* compared with the conventional single U-tube, which is always more than zero. Q_H and $V\Delta P$ are the heat exchange rate and pumping power, respectively. Q'_H and $\Delta P'$ are the increment of the heat exchange rate and pressure drop, respectively, compared with the single U-tube.

5. Design optimization

Many articles had proposed different configurations of GHX to improve GSHP systems' performance, as mentioned in the Introduction. However, most of these studies focused only on changing the designs other than optimizing the design parameters (geometrical or operating parameters) such as spiral diameters, pitch distance, tube diameter, grout thermal conductivity, and fluid flow rate. The present study fills this gap and proposes new optimization methods using the design exploration tool introduced by the ANSYS workbench.

The design exploration algorithm optimizes the design variables based on the constraints of each parameter and defined objective functions. The optimization process begins with the initial sampling step via the DOE. The interpolation is then performed based on the Kriging algorithm in the response surface method step. Finally, the optimization is conducted with data obtained from the preceding two steps using the multi-objective genetic algorithm (MOGA). These steps are explained in detail in the following subsections.

5.1. Design of experiments (DOE)

The DOE randomly generates sampling points most efficiently with a minimum number of sampling points. The efficient distribution of the sampling points increases the accuracy of the response surface. The number of sample points filling the design space depends on the input parameters and their spans. The central composite design algorithm is the deterministic method used in this step, combining one center point, points along the axis of the input parameters, and the points defined by the fractional factorial design. Therefore, the total number of design points in this study was 75 points [29], as shown in **Fig. 9.**

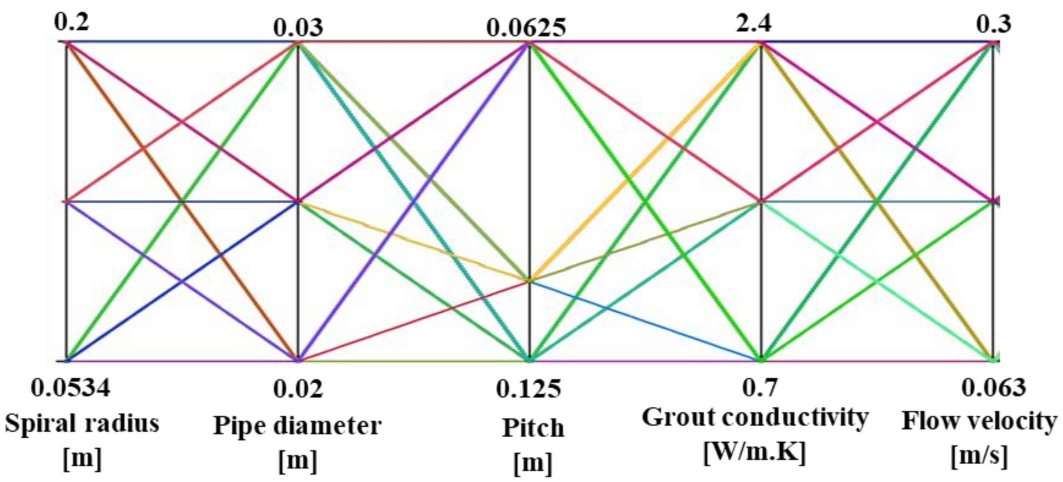

Fig. 9. Parallel chart of parameters

In this study, the design variables were classified as continuous and discrete variables. The spiral radius, grout thermal conductivity, and fluid inlet velocity were continuous, with ranges indicated in **Table 5.** Simultaneously, the pipe diameter and pitch distance are considered discrete variables with three values, as listed in **Table 5.**

Table 5 Design variables classifications and their ranges and values

Variable	Classification	Range		Value
		from	to	
Spiral radius (m)	Continuous	0.0535	0.2	-
Grout conductivity (W/m.K)	Continuous	0.7	2.4	-
Fluid inlet velocity (m/s)	Continuous	0.063	0.3	-
Pitch (m)	Discrete	-		0.125, 0.1, 0.0625
Pipe diameter (m)	Discrete	-		0.02, 0.026, 0.03

5.2. Response surface method (RSM)

The response surface allows the design and understanding of the variation of the output parameters by the change in the input parameter, which can be used efficiently to modify the design and yield improved performance. The accuracy of the response surface depends mainly on the choice of the response surface algorithm, the complexity of the solution variations, and the number of design points generated during the design of the experiment [33]. The Kriging meta-modeling algorithm provides an improved response quality by utilizing the multidimensional interpolation polynomial regression model in the present study. It produces correlations between the input and output parameters, as shown in Eq. (18)[34].

$$f = \beta_0 + \sum_{j=1}^{n} x_j + \sum_{j=1}^{n} \beta_{jj} {x_j}^2 + \sum_{i=1}^{n} \sum_{j=1, i\neq j}^{n} \beta_{ij} x_i x_j \quad (18)$$

where f is the response, $\mathcal{X}$ is the design variable, n is the number of design variables, and $\beta_0, \beta_i, and\ \beta_j$ are the regression coefficients.

4.3. Goal-driven optimization

There are two types of goal-driven optimization systems: response surface optimization and direct optimization. The response surface optimization method used in this study derives information from the response-surface step. In this study, the multi-objective optimization algorithm (MOGA) using the Pareto optimal solution was applied to optimize the design variables fulfilling the target sets by maximizing both the *COP*_improvement (Eq. 17) and net thermal heat gain (Eq. (11)). MOGA is an evolutionary algorithm with several objective functions that are optimized simultaneously; notably, they are subject to inequality and equality constraints[33]. It initially generates 5000 samples, 1000 samples per iteration, and finds three candidates in a maximum of 20 iterations. **Figure 10** shows the workflow of the optimization process used in this study.

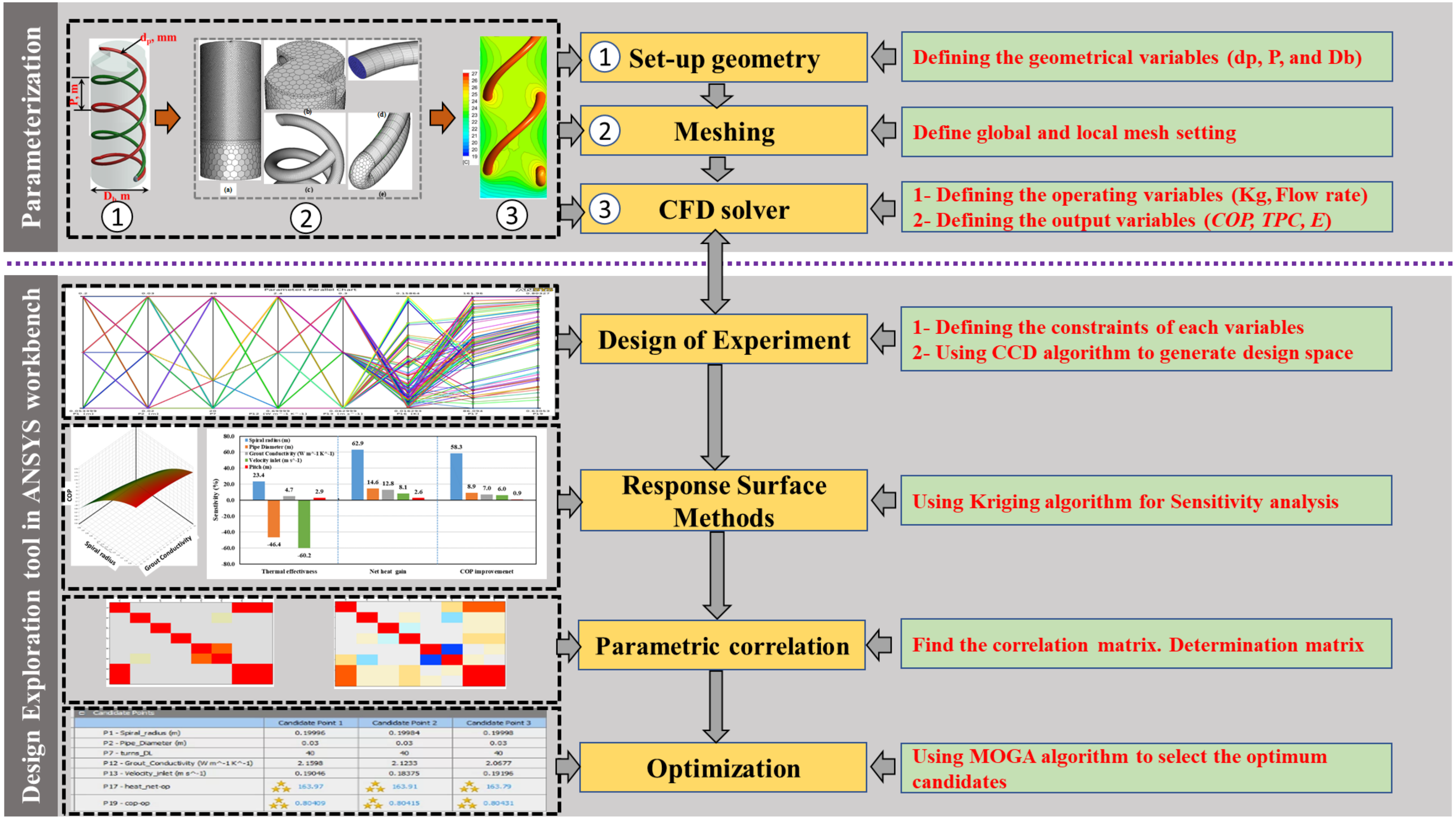

Fig. 10. Flow chart of optimization process used in this study

6. Results and discussions

This paper proposes a new spiral-double GHX as an improvement in the heat transfer inside a customary helical ground heat exchanger used for GSHP systems. The numerical results of the spiral-double GHX were compared with those of the spiral GHX. Transient simulations were conducted, and the results are discussed in the following.

6.1.Numerical results validation

To validate the numerical results, the transient simulation results of the typical single U-tube spiral GHXs were compared with the results presented by **Jalaluddin et al. [6]**. Jalaluddin et al. [6] developed a transient and three-dimensional numerical model to simulate the heat transfer inside the single U-tube and spiral GHX with a depth of 20 m, a spiral diameter of 0.1398 m, and a pitch of 0.2 m. Additionally, the transient simulation was conducted for 72 hours.

In the present study, the average value of the fluid outlet temperatures and the total heat exchange rate from the GHX to the surrounding soil was calculated after 24, 48, and 72 h and compared with the numerical results presented in Ref. [6], as shown in **Fig. 11 and 12**, respectively. Moreover, two flow rates of 2 L/min and 8 L/min, which correspond to laminar and turbulent flow conditions, were investigated. **Figures 11a and c** show the differences between the fluid outlet temperature and heat exchange rate calculated from the current study and those calculated from Ref. [6] for a single U-tube under laminar and turbulent flow conditions. A good agreement is observed in the outlet fluid temperature with an average error value of -0.13 ºC, and -0.04 ºC for laminar and turbulent flow conditions, respectively. In addition, the error percentage of the heat exchange rate was 5.3 % for laminar flow and 4.9 % for turbulent flow conditions, as shown in **Fig. 11b and d.**

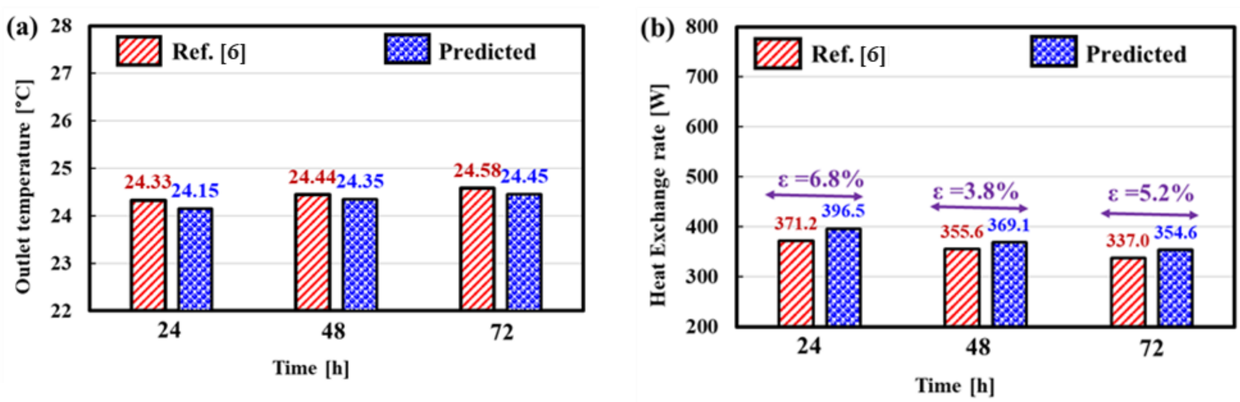

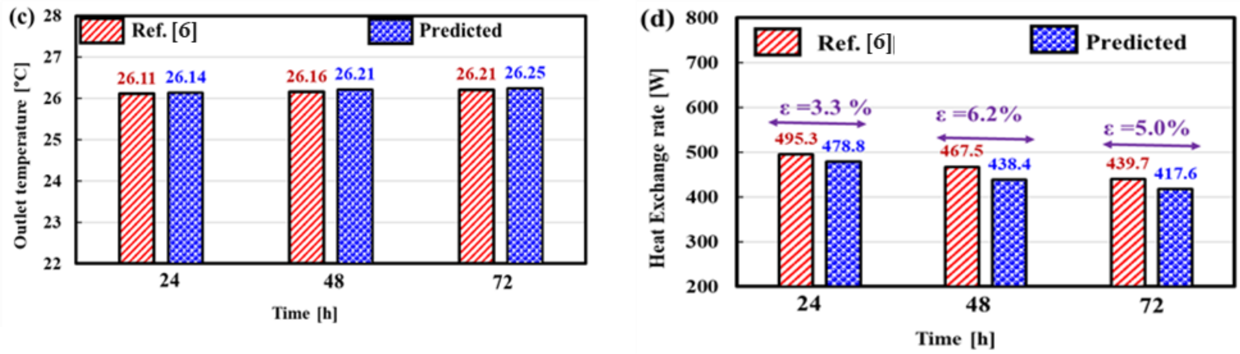

Fig. 11. Comparison of current predicted results with the numerical results indicated by [6] for single U-tube GHX at (a) fluid outlet temperature under the flow rate of 2 L/min, (b) heat exchange rate under the flow rate of 2 L/min, (c) fluid outlet temperature under the flow rate of 8 L/min, and (d) (b) heat exchange rate under the flow rate of 8 L/min

In addition, **Fig. 12a and c** indicate the same agreement with an average error value of -0.15 °C and -0.05 °C for laminar and turbulent conditions, respectively, for the spiral GHX. The error percentage in the heat exchange rate was 4.6 % for laminar and turbulent flows, as shown in **Fig. 12b and d.** These results illustrate that the present numerical model achieved high accuracy under turbulent and laminar conditions.

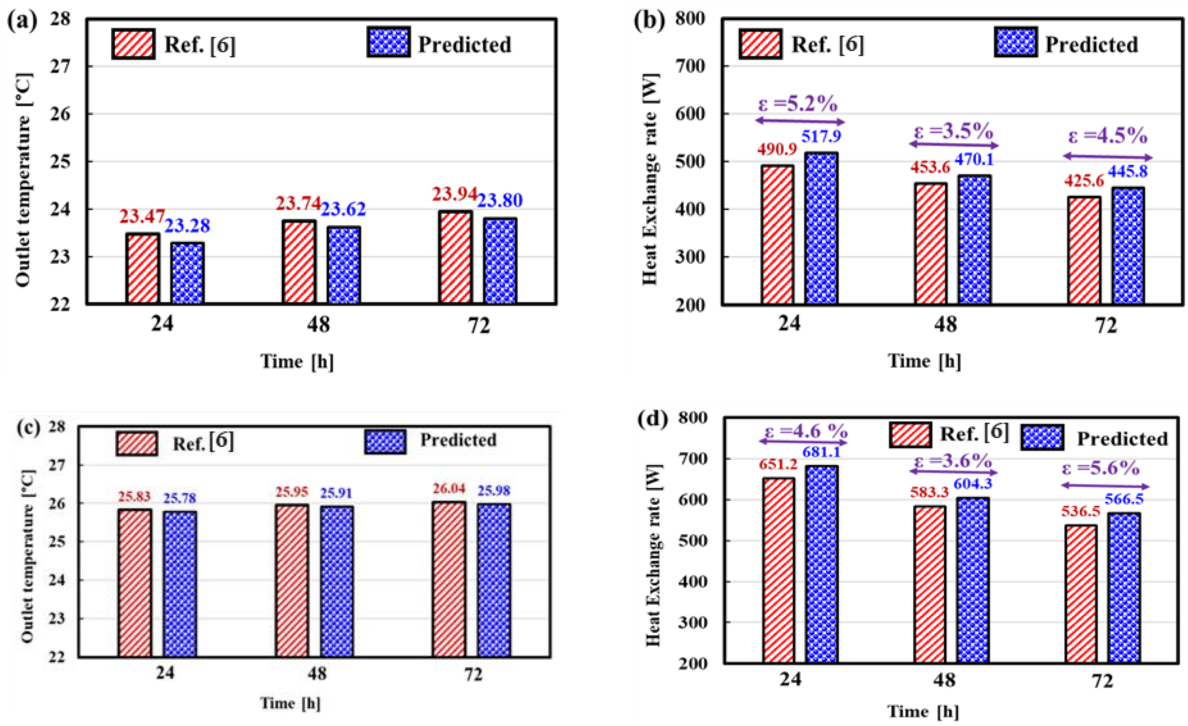

Fig. 12. Comparison of current predicted results with the numerical results indicated by [6] for spiral GHX at (a) fluid outlet temperature under the flow rate of 2 L/min, (b) heat exchange rate under the flow rate of 2 L/min, (c) fluid outlet temperature under the flow rate of 8 L/min, and (d) (b) heat exchange rate under the flow rate of 8 L/min

After validating the numerical model, the transient thermal responses of a single U-tube and spiral GHX with spiral-double GHXs were compared.

6.2. Comparison results

The thermo-hydraulic performance comparison between the typical single U-tube, spiral, and spiral-double GHX was carried out numerically under transient conditions and two different fluid flow rates. The three GHXs have dimensions, as shown in **Fig. 6.** The thermal effectiveness (*E*), pressure drop, heat transfer rate (*Q*), net heat transfer rate (Q_{net}), *TPC*, and *COP_* improvement were calculated and analyzed.

6.2.1. Thermal effectiveness and pressure drop

Figure 13 compares the thermal effectiveness (*E*) and pressure drop of the three GHXs at two flow rates of 2 and 8 L/min. *E* decreases with increasing flow rate as the outlet fluid temperature decreases with increasing flow rate. This is because the fluid does not have sufficient time to exchange heat with the surrounding soil. In addition, the spiral double GHX shows higher *E* values compared with other GHXs, causing the coils and turns to enhance the heat transfer from the surrounding soil to the flowing fluid. Moreover, the *E* value of the spiral-double GHX is 0.12, compared with 0.08, which is 50 % higher for a flow rate of 8 L/min. The difference decreases to 31.6 % flow rate of 2 L/min. However, it shows an improvement of 4.6 % and 11.0 % compared with the spiral GHX for flow rates of 2 and 8 L/min.

In contrast, the pressure losses encountered inside the spiral and spiral-double GHXs are always higher than those inside the single-U-tube GHX for all flow rates. The pressure losses increased with increasing flow rate, and the spiral double GHX showed the highest values. The reason for that results is that the spiral-double GHX has a large number of turns and curves compared with the spiral GHX, which has half coils, while the single-U tube has a straight pipe. Coils cause more friction with the tube surface and, accordingly, more flow resistance.

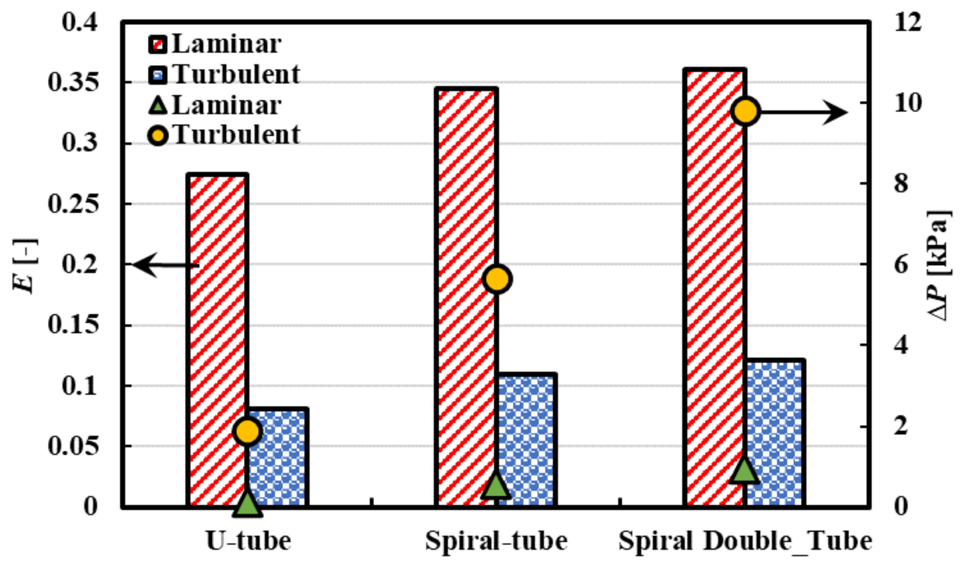

Fig. 13. Effectiveness comparison between single U-tube, spiral, and spiral-double GHXs

6.2.2. Temperature contours

Figure 14 presents the temperature distribution contours in the longitudinal planes at the upper and bottom regions and the horizontal planes at a depth of 10 m for a flow rate of 8 L/min. These figures show distinct differences among the three GHXs. In the upper region, in the case of single-U tubes, the temperature distribution through grout appears to be approximately symmetrical around the vertical tube, which is not apparent in the spiral and spiral-double GHXs. The temperature gradient is more prominent around the lower leg tube because of the higher temperature difference of 2 °C, while it is 0.5 °C around the upper leg tube. Moreover, the thermal interference between the two coils turns more significant in the spiral GHX than in the spiral-double GHX owing to the close distance between the helical down leg and the straight-up leg tube.

In the bottom part, this region is colored with a stratified temperature from the cold bottom surface at a temperature of more than 19 °C to a higher temperature of 25 °C inside the grout domain and 26.5 °C inside the fluid material.

Nevertheless, the horizontal planes at depths of 10 m show some differences among the three GHXs. At a depth of 10 m, the spiral GHX had an eccentric temperature distribution in the radial direction around the inlet pipe. The temperature difference between the fluid and surrounding grout was 4 °C. However, the temperature differences are 2.5 ºC and 3.2 ºC in the spiral-double GHX and identified by a temperature distribution pattern. In addition, the single-U tube GHX shows a distribution with concentric temperature contour lines that are more concentrated around downward tubes than upward tubes.

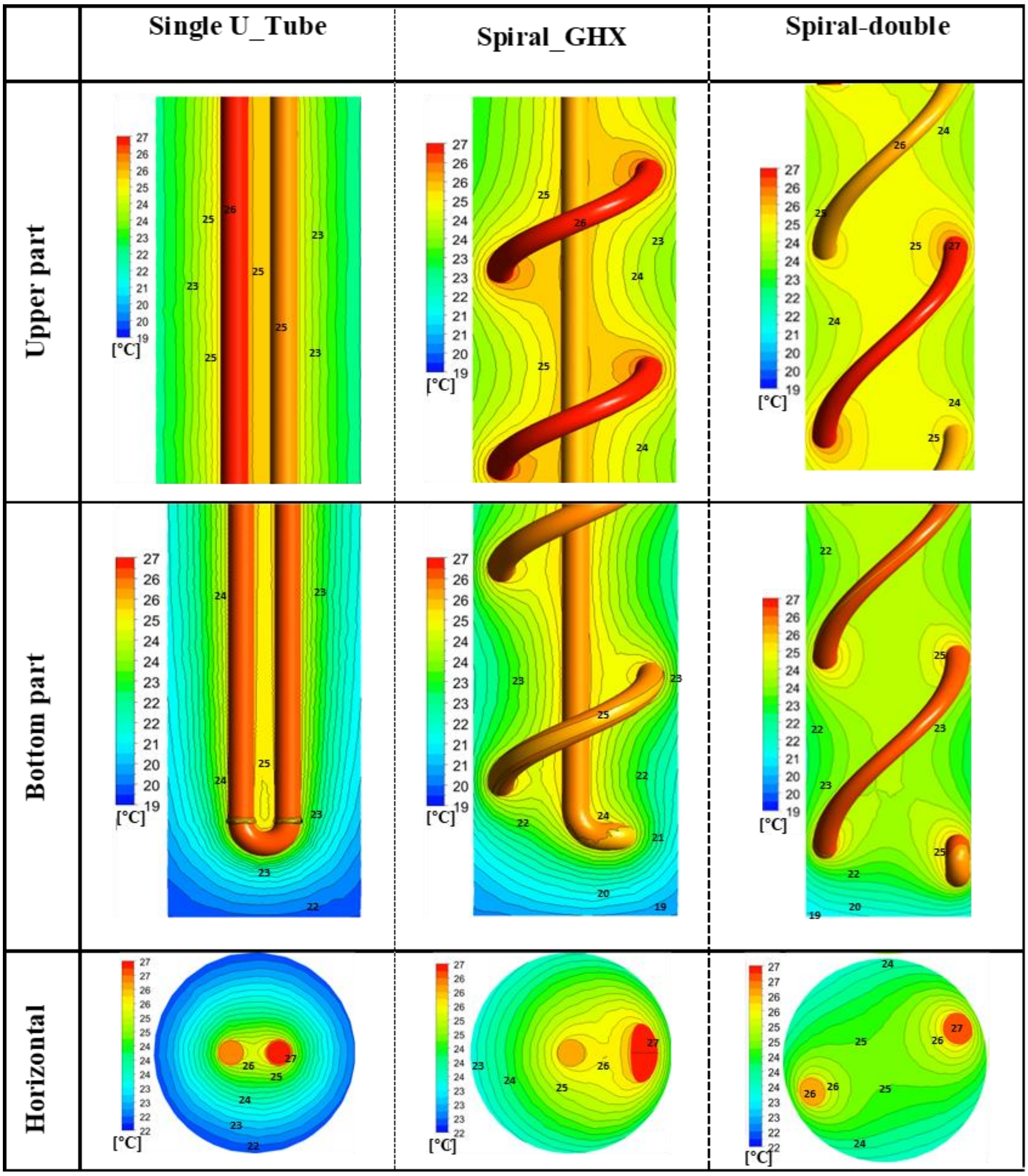

Fig. 14. Temperature contours in longitudinal and lateral planes at depths of 10 m

6.2.3. Fluid temperature profile

The fluid temperature profiles inside the down leg and up leg tubes at flow rates of 2 and 8 L/min are shown in **Fig. 15a and b.** In all cases, the inlet temperature was maintained at 27 °C (300.15 K). **Figure 15** shows that the outlet temperature decreases along the tube length because of the rejection of heat energy from the surrounding soil. For the single-U tube, the temperature declines by 1.7 K and 0.4 K through the down leg for a flow rate of 2 and 8 L/min, respectively, and it decreases by 0.79 K and 0.35 K through the up leg. For the spiral GHX; the temperature drops by 3.01 K and 0.8 K while passing inside the down leg for 2 and 8 L/min flow rates.

Moreover, the temperature decreases by 0.19 K and 0.18 K when the effluent passes through the upper leg for laminar and turbulent flow conditions, respectively. This decrement is because the down-leg tube has a longer path than the up-leg tube's straight path. Finally, the spiral-double GHX shows an approximately equal increment of 0.6 K through the up-leg and down-leg tubes, especially under higher flow rates of 8 L/min. However, at a flow rate of 2 L/min, the lower leg tubes show a higher temperature difference (2.8 K) compared with 0.73 K). Finally, the average fluid temperature increased with increasing flow rate. Resembling the spiral and spiral-double GHX, the downleg tube of the spiral GHX is longer than that of the spiral-double GHX. Simultaneously, the up-leg tube of the spiral-double GHX is longer than that of the spiral GHX, which causes the temperature gradient shown in Fig. 14a and b.

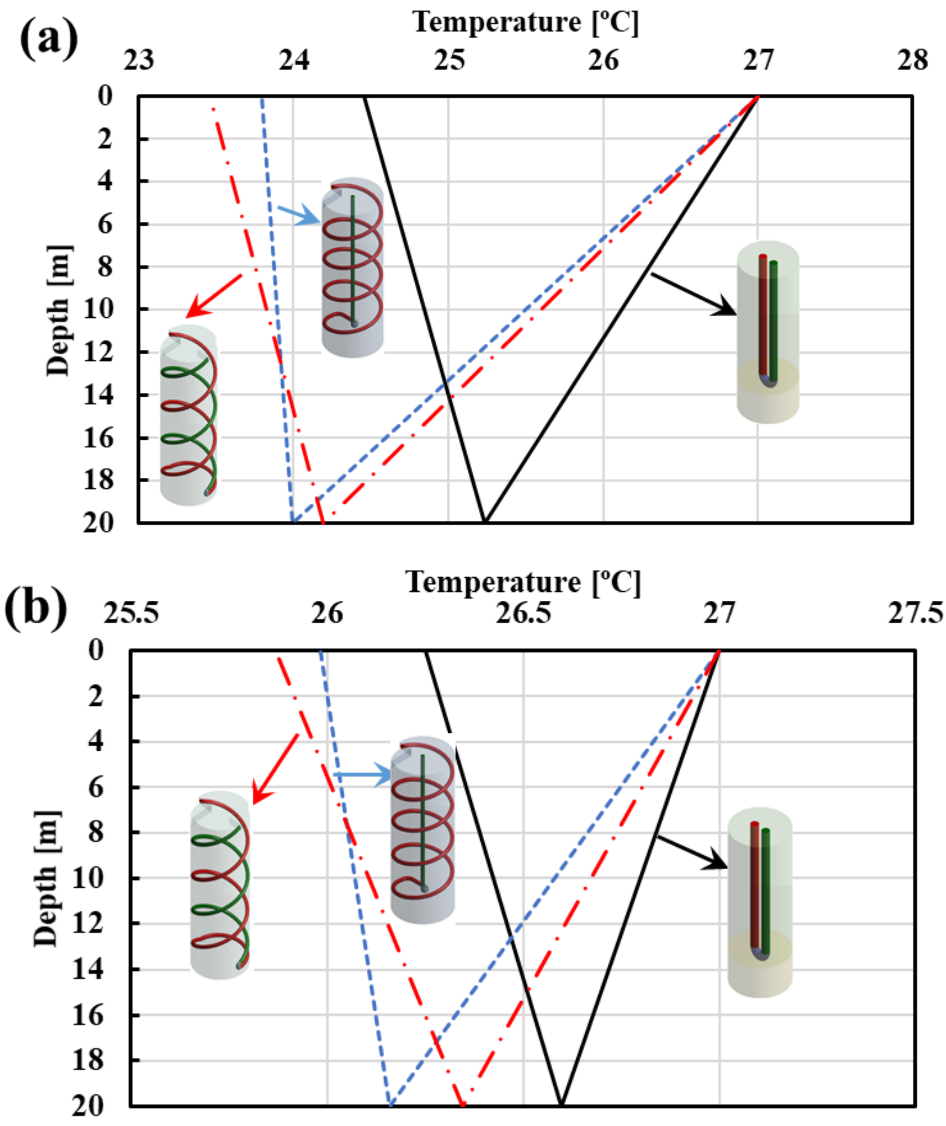

Fig. 15. Fluid temperature profile comparison for (**a**) laminar and (b) turbulent flow conditions

6.2.4. Heat transfer rate in the DL and UL of the GHX

The heat energy transferred to the surrounding soil and rejected via the DL and UL of the single-U tubes, spiral, and spiral-double GHX at flow rates of 2 and 8 L/min are shown in **Fig. 16.** Figure 16 shows that more than 70 % and 50 % of the total heat energy through the single-U tube GHX are rejected from the DL for laminar and turbulent flow conditions. Furthermore, more than 90 % and 80 % of the total heat energy via the spiral GHX were dissipated via the UL tube at flow rates of 2 and 8 L/min. Although the spiral-double GHX presented a moderate heat transfer rate from each leg with a higher flow rate, it shows that DL rejected less than 57.8 % of the total heat energy for a flow rate of 8 L/min.

For a clearer analysis, the total heat energy and net heat energy calculated using Eq. (11), as shown in **Fig. 17.** The spiral-double GHX rejected the highest amount of 493 W and 628.9 W for flow rates of 2 L/min and 8 L/min, respectively. While the net heat energy is 492.8 W and 620.5 W, the thermal heat energy required to drive the pump is 0.2 W and 8.4 W, respectively. In the same context, the net heat energy absorbed via spiral-double GHX is 47 W and 59 W more than that of the spiral GHX at flow rates of 2 L/min and 8 L/min, while the difference is 138.3 W and 204.7 W compared with the single U-tube, as shown in **Fig. 17.**

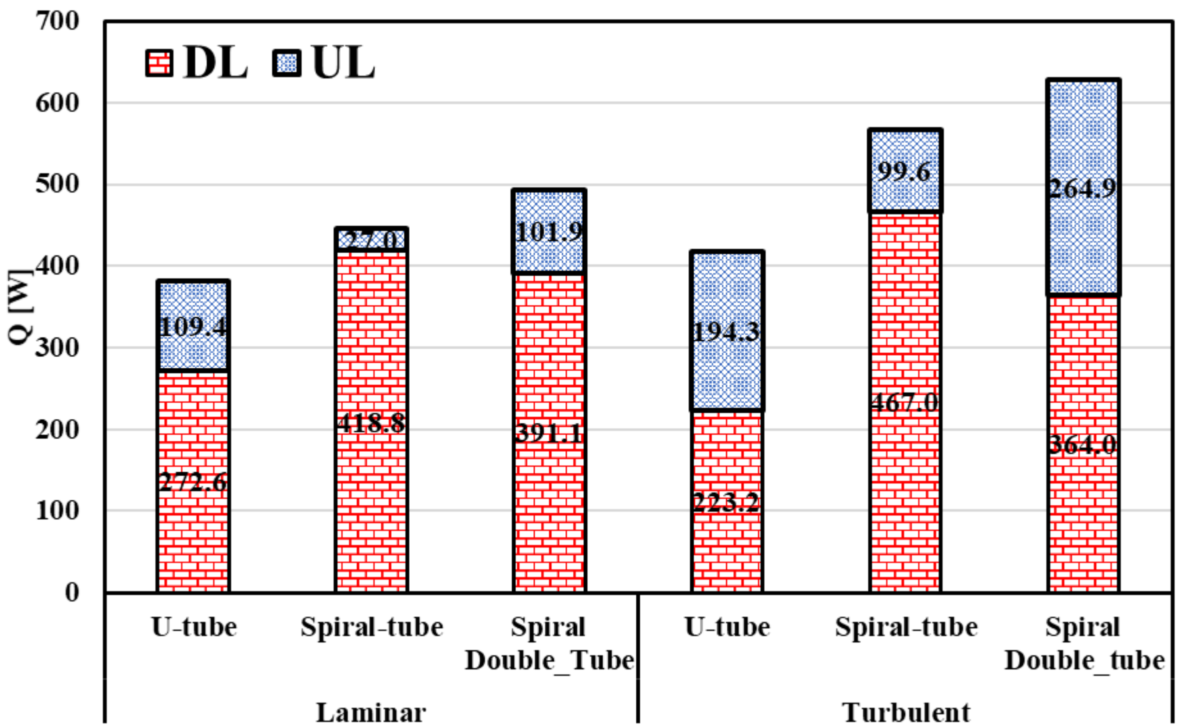

Fig. 16. Heat transfer rate in each tube leg for flow rates of laminar and turbulent flow conditions

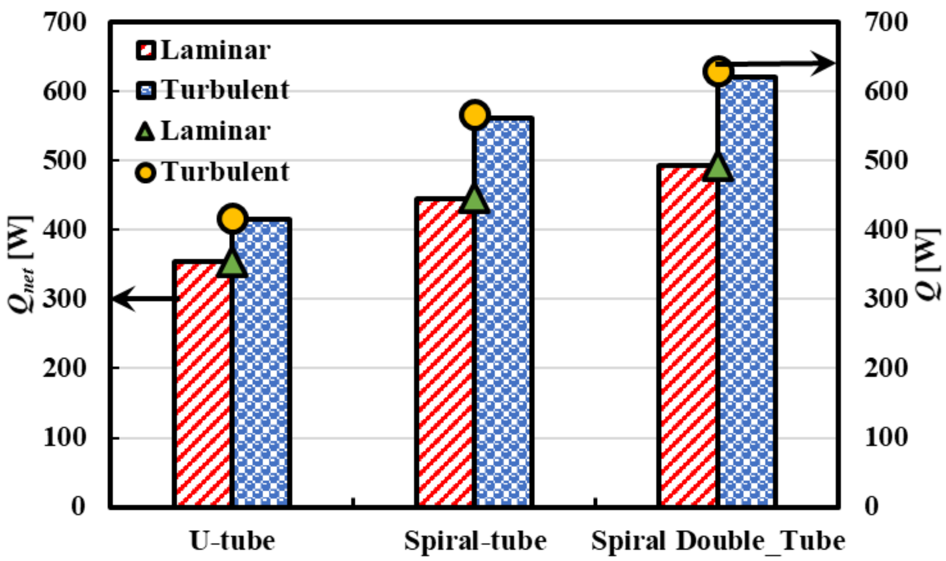

Fig. 17. Total and net heat energy rejected by GHXs under different flow rates

6.2.5. Thermal performance capability (*TPC*) and *COP* improvement

The *TPC* is an indicator of the performance that combines the thermal and hydraulic performance compared with the primary case, the single-U tube GHX. A *TPC* value of more than 1 indicates that the *TPC* value is greater than that of the single-U tube GHX, which illustrates the advantage of thermal effectiveness compared to the hydraulic pressure drops. **Figure 18** shows the *TPC* of the spiral and spiral-double GHXs for the two flow rates. For laminar flow, the spiral and spiral-double GHXs have a *TPC* of 0.89, and 0.76, respectively, which affirms that the thermal effectiveness is less beneficial with the consumed pressure drop. However, this value increased dramatically with increasing flow rate because of the enhanced heat energy rejected to the surroundings compared with the required pumping pressure to compensate for the friction losses. The *TPC* increases to 1.12 and 0.99 when flow rates increased to 8 L/min for spiral and spiral-double GHXs, respectively. Conversely, the *COP* improvement calculated from Eq. (17) is shown in **Fig. 18.** The spiral-double GHX shows a better *COP* improvement of 0.4 and 0.5 for laminar and turbulent flow conditions compared with 0.26 and 0.36 for spiral GHX, respectively.

These results confirm that the spiral-double GHX has the advantage of improving the *COP* of the GSHP system compared with the single U-tube and spiral GHX, indicating its applicability as an effective alternative to conventional GHXs.

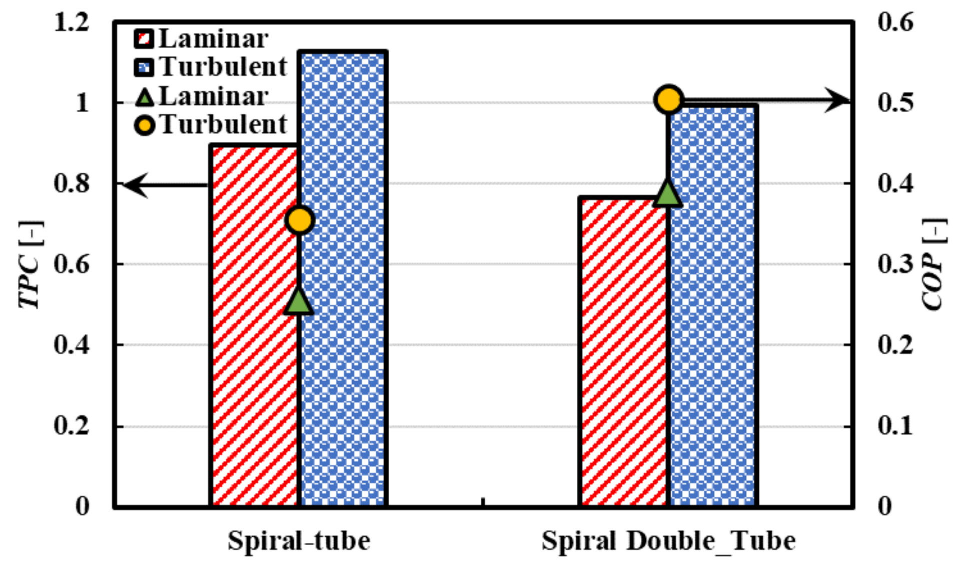

Fig. 18. Comparison of TPC and *COP* improvement between spiral and spiral-double GHXs under different flow rates

6.2.6. Thermal resistance (R_b)

Figure 19 shows the total thermal resistance (R_b) of the borehole calculated using Eq. (13). A lower thermal resistance indicates a higher possibility of heat transfer from the flowing fluid toward the soil through the grouting and pipe materials. The figure shows that the spiral double has the lowest *Rb* for all flow rates, with R_b being 0.084 and 0.054 m · K/W for 2 and 8 L/min, respectively. Therefore, spiral-double reduces R_b by 66.9 % and 75.3 % compared with the single-U-tube GHX for different flow rates. Moreover, R_b was reduced by 35.9 %and 44.8 % compared with that of the spiral GHX due to the improved heat transfer

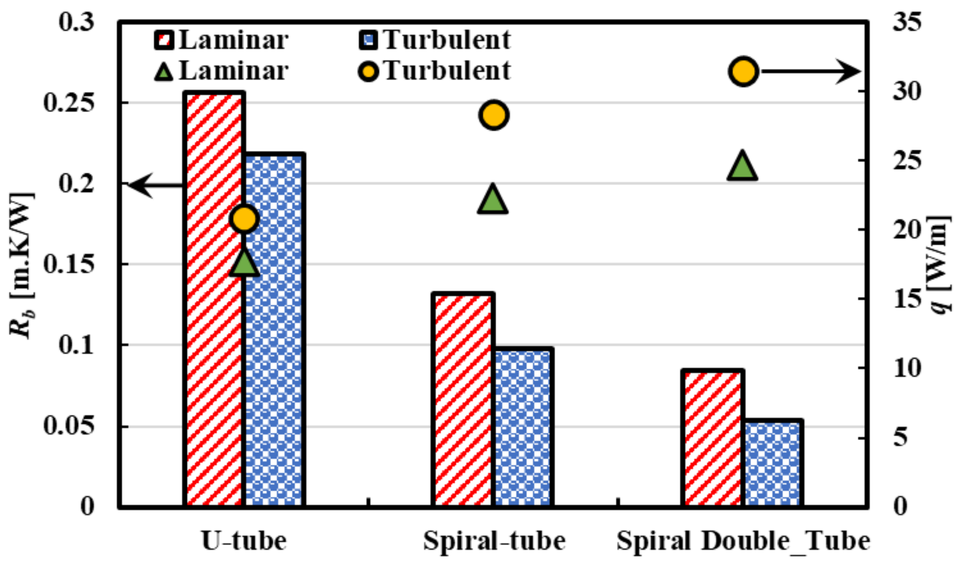

Fig. 19. Thermal resistance of single-U tubes, spiral, and spiral-double GHXs at different flow rates

rate, as shown in Fig. 18. Although these results demonstrate the possible enhancement that can be achieved by using spiral-double GHX, it requires further investigation based on the long-term and short-term periods under cooling/heating loads with a dynamic attitude. These further investigations will be fundamental for future studies.

6.3. Parametric analysis results

The particular impact of operating, geometrical, and geological parameters on the *E*, *TPC*, *COP*, and R_b, and fluid temperature distribution were investigated as part of the parametric analysis. The operating conditions are presented by flow rates of 2 and 8 L/min, while the geometrical conditions include four pitch distances (*P*), three tube diameters (d_p), and four borehole diameters (D_p). The geological conditions included three grouting materials. Descriptions of the 12 cases are listed in **Table 4.** The results for each parameter are explained in the following subsections.

6.3.1. Pitch distance impact

The pitch distance was changed from 0.05, 0.1, 0.15, and 0.2 m, while the other parameters were kept constant. Increasing the pitch distance results in a decrease in the total tube length and a consequent decrease in the total heat transfer area; consequently, the heat transfer rate also decreased, and the pressure drops also decreased, as shown in **Fig. 20c.** Furthermore, the net heat transfer (Q_{net}) was reduced by 9.7 %, from 621.08 W to 561.43 W. Doubling the pitch from 0.1 m to 0.2 m, reducing the tube length from 92.1 m to 51.8 m, cutting down the surface area from 7.52 m^2 to 4.23 m^2. In addition, *E* shows changes with a value of 9.7 %, while *TPC* and *COP* decrease by 17.7 % and 29 %, respectively, and R_b increases by 100 %, as shown in **Fig. 20a, b, and d,** while the fluid exit temperature increases by 0.11 K, as shown in **Fig. A1 in Appendix A.** Moreover, the temperature distribution of the grouting materials is presented in **Fig. 21.** The temperature decreased in the radial direction, increasing the pitch distance as the fluid outlet temperature increased with increasing thermal resistance.

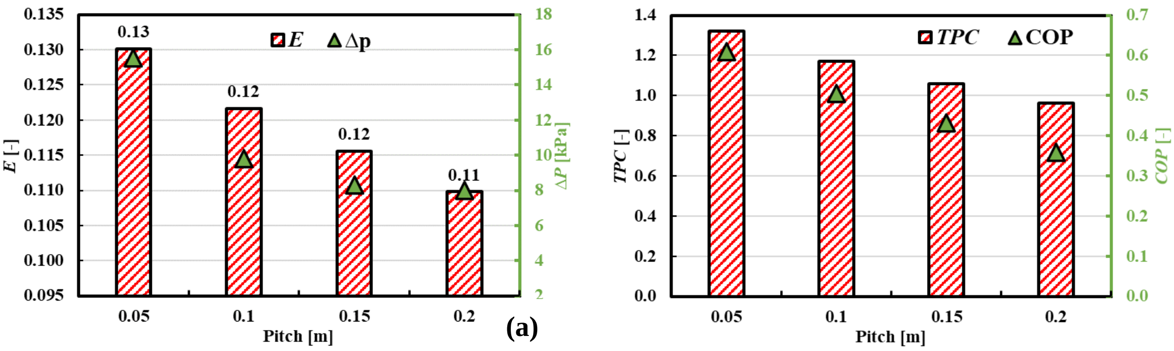

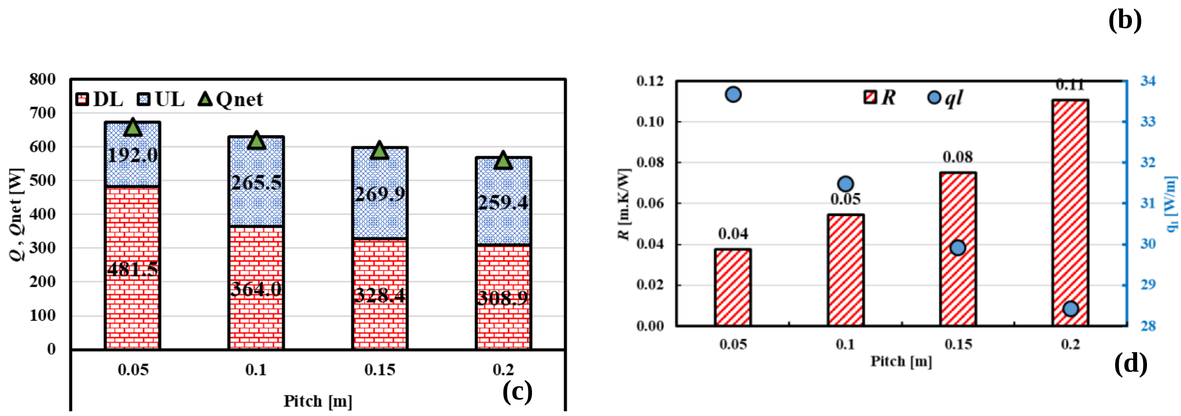

Fig. 20. Impact of four-pitch distances on (a) E and ΔP, (b) *TPC and COP*, (c) *Q and Qnet* and (d) R and q_l

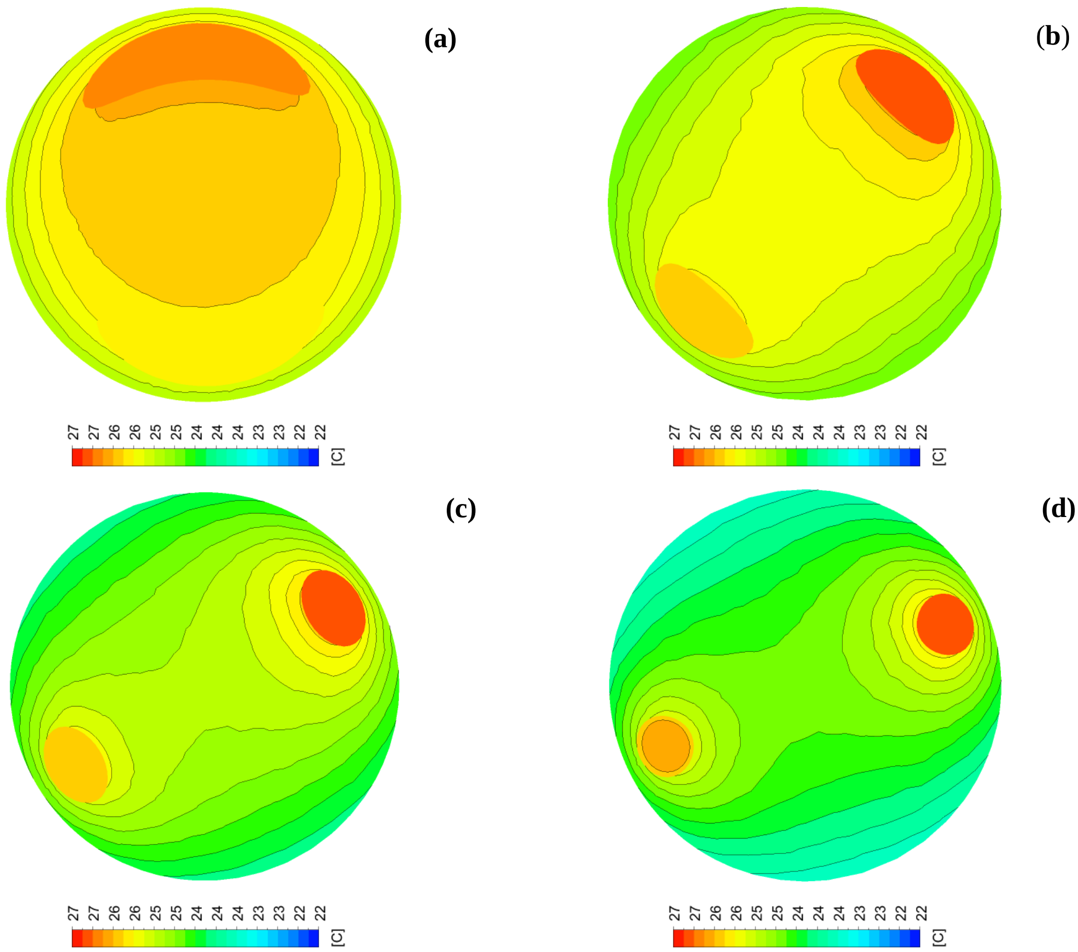

Fig. 21. Temperature contours on a horizontal plane at a 10 m depth for a) 0.05 m, b) 0.1 m, c) 0.15 m, and d) 0.2 m pitch

6.3.2. Flow rate impact

The effects of two flow rates (2 and 8 L/min) on *E*, *TPC*, *COP*, and R_b are shown in **Fig. 22**. Increasing the flow rate from 2 to 8 L/min decreased *E* by 68.1 %, increased *TPC* by 22.8 %, increased *COP* by 29.1 %, and decreased R_b by 36.3 %, and also increased the outlet fluid temperature from 23.5 °C to 25.9 °C, as shown in **Fig. A2 in Appendix A**. The total heat transfer rate was increased by 27.6 % from 493.01 W to 628.95 W, and the Qnet was increased by 26.9 % from 492.9 W to 625.8 W, as indicated in **Fig. 22c. Fig. 23.** indicates that the grout temperature increased with increasing flow rate because a higher flow rate promotes heat transfer rate exchange in the surrounding material.

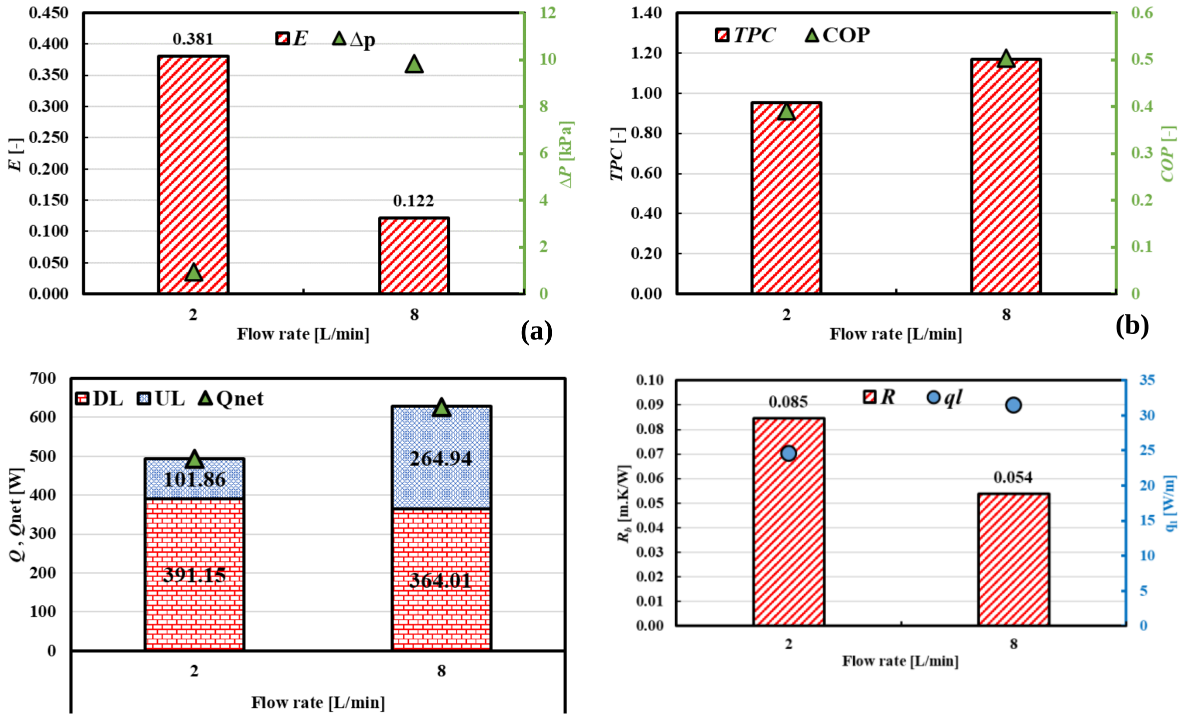

Fig. 22. Effect of different flow rates on (a) E and ΔP, (b) *TPC and COP*, (c) *Q and Qnet* and (d) R and q_l

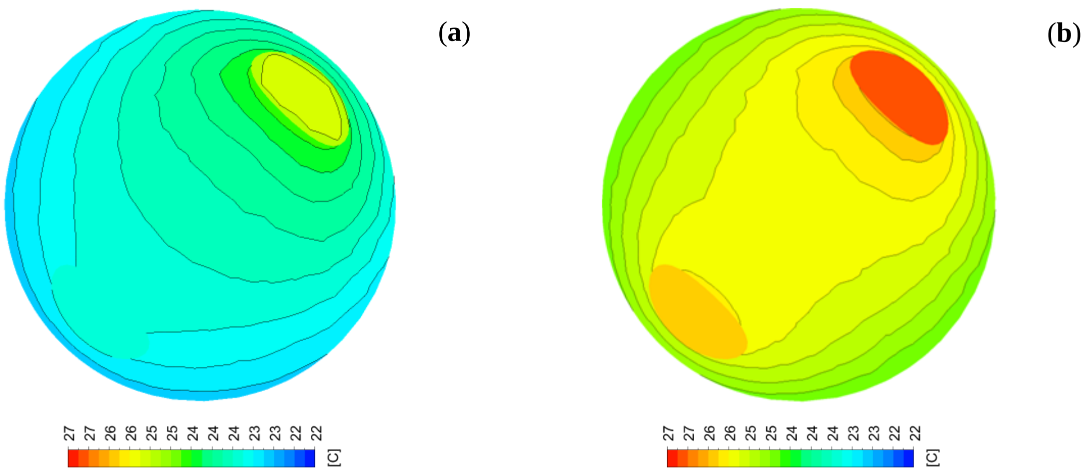

Fig. 23. Temperature contours on a horizontal plane at a 10 m depth at (a) 2 L/min and (b) 8 L/min

6.3.3. Tube diameter effect

Three tube diameters (20, 26, and 30 mm) were examined in this study. Increasing the diameter decreased the outlet temperature and friction factor, consequently increasing *E* by 4.4 %, increased *COP* by 15.6 %, decreased *TPC* by 6.2 %, and decreased R_b by 27.9 %, as shown in **Fig. 24.** Due to the increase in the heat transfer area and reduction in friction losses, the net heat transfer rate increased by 8.4 %, as shown in **Fig. 24c.** The fluid outlet temperature demonstrated a negligible increase, as shown in **Fig. A3 in Appendix A.** Grout temperature increased gradually with increasing pipe diameter, as shown in **Fig. 25.**

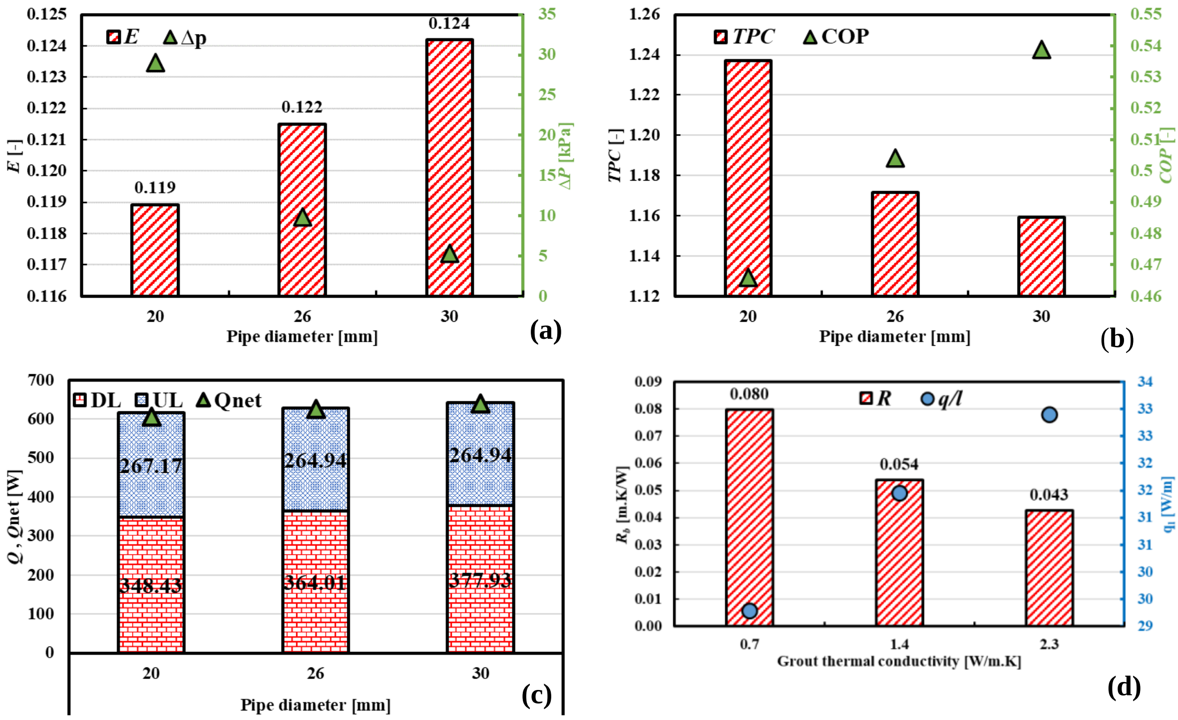

Fig. 24. Impact of tube diameter on (a) *E* and Δ*P*, (b) *TPC and COP*, (c) *Q and Qnet* and (d) *R* and q_l

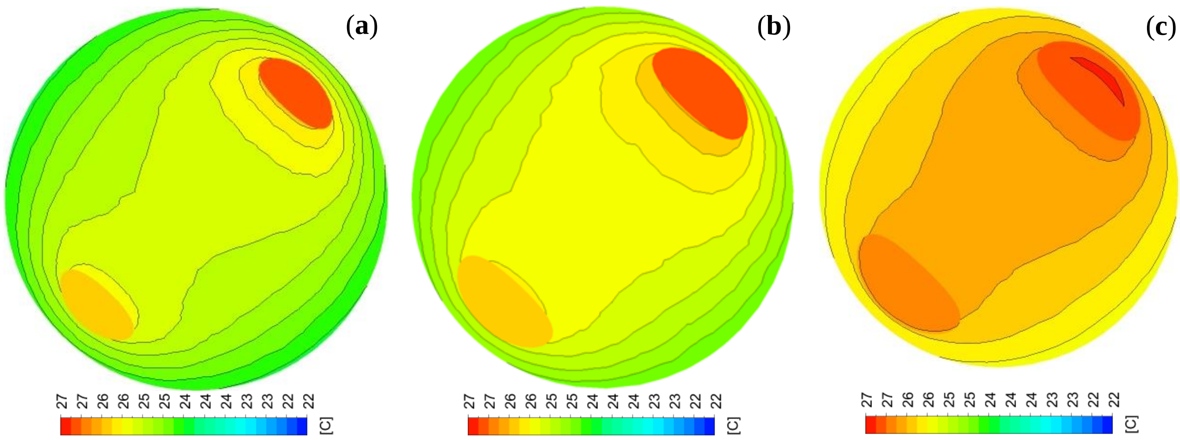

Fig. 25. Temperature contours on a horizontal plane at a 10 m depth at a (a) 20, (b) 26, and (c) 30 mm tube diameter

6.3.4. Grout material impact

The grout material's thermal conductivity (K_g) varied from 0.7, 1.4, and 2.3 W/m.K. Increasing the borehole's thermal conductivity increases the net heat transfer rate by 12.4 %, from 582.42 W to 654.78 W, as indicated in **Fig. 26c.** Moreover, R_b is decreased by 46.6 %, *COP* increases by 43.3 %, while *E* and *TPC* are increased by 12.4 %, as indicated in **Fig. 26a and b.** However, the fluid outlet temperature decreased by 0.13 °C when K_g rose from 0.7 to 2.3 W/m.K, as shown in **Fig. A4 in Appendix A**. Consequently, the surrounding grout temperature increased, as shown in **Fig. 27.**

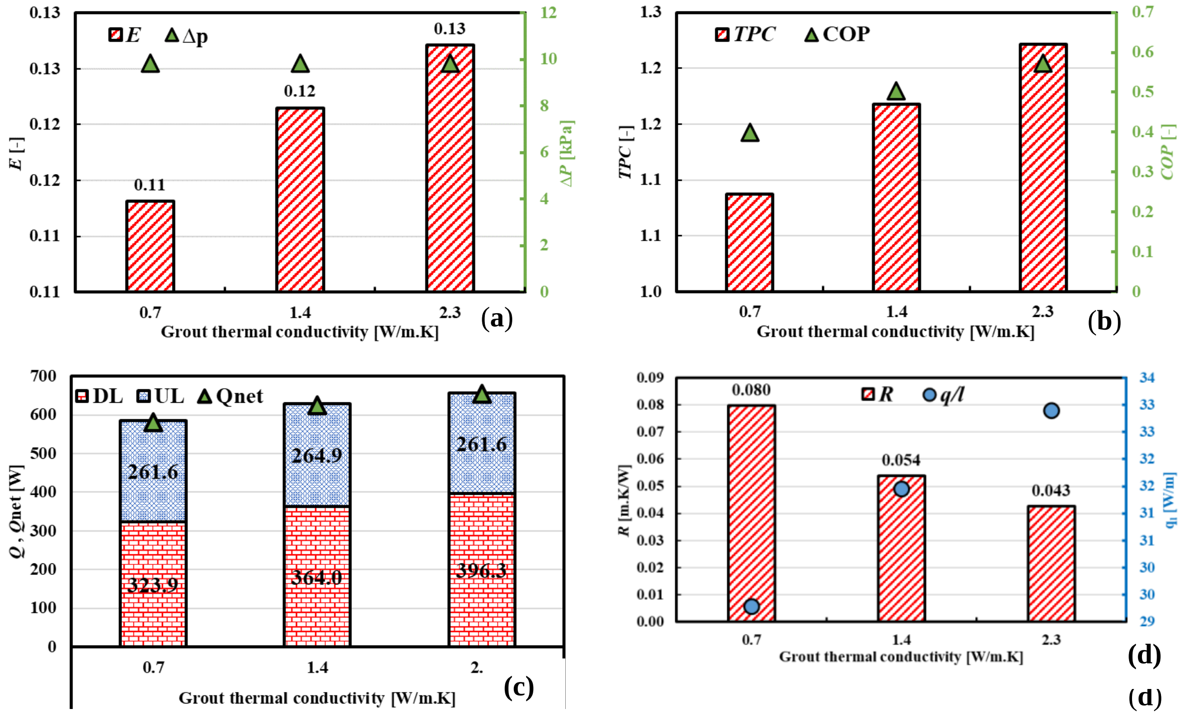

Fig. 26. Impact of grouting thermal conductivities on (a) *E* and Δ*P*, (b) *TPC and COP*, (c) *Q and Qnet* and (d) *R* and q_l

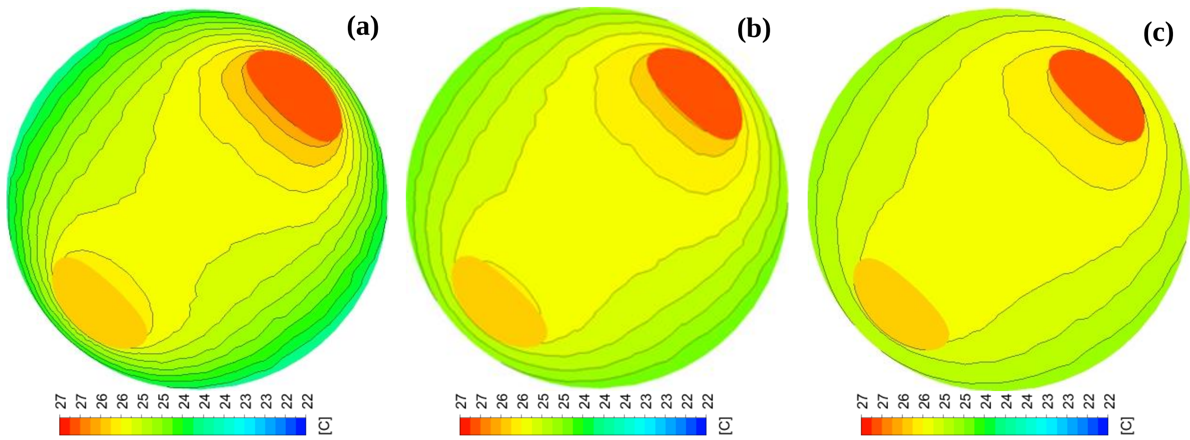

Fig. 27. Temperature contours on a horizontal plane at a 10 m depth at different grout

conductivities: (a) 0.7, (b) 1.2, and (c) 1.5 W/m.K

6.3.5. Spiral diameter

Four spiral diameters of 0.14, 0.2, 0.26, and 0.32 m were also simulated; increasing spiral diameters were expected to increase the heat transfer area and the total and net heat transfer rate, as listed in **Fig. 28.** The Q_{net} increases by 46.8 % from 625.8 W to 918.4 W, while the *E*, *COP*, and *TPE* also increases by 46.7 %, 139.3 %, and 68.1 %, respectively, and R_b decreases by 45.8 % from 0.05 m.K/W to 0.03 m.K/W, as shown in **Fig. 28. Figure A5 in Appendix A** illustrates that the fluid exit temperature drops from 25.9 °C to 25.3 9 °C, which results in an increase in the surrounding grout temperature, as shown in **Fig. 29.**

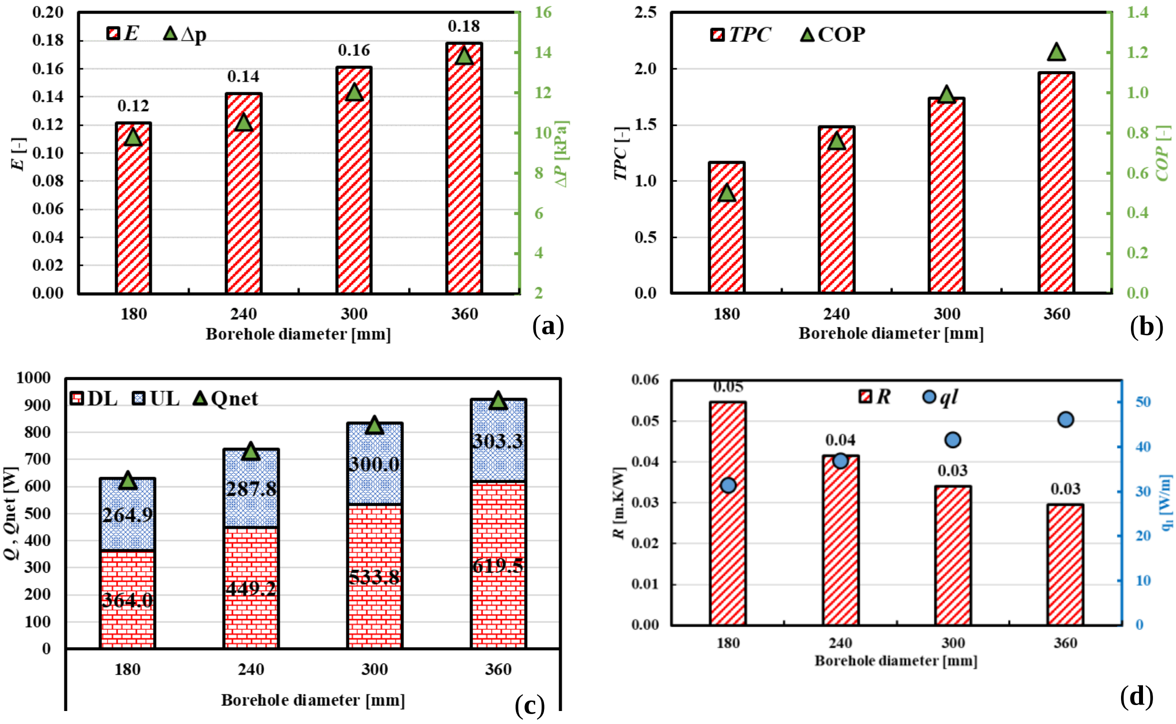

Fig. 28. Impact of borehole diameter on (a) *E* and Δ*P*, (b) *TPC and COP*, (c) *Q and Qnet* and (d) *R* and q_l

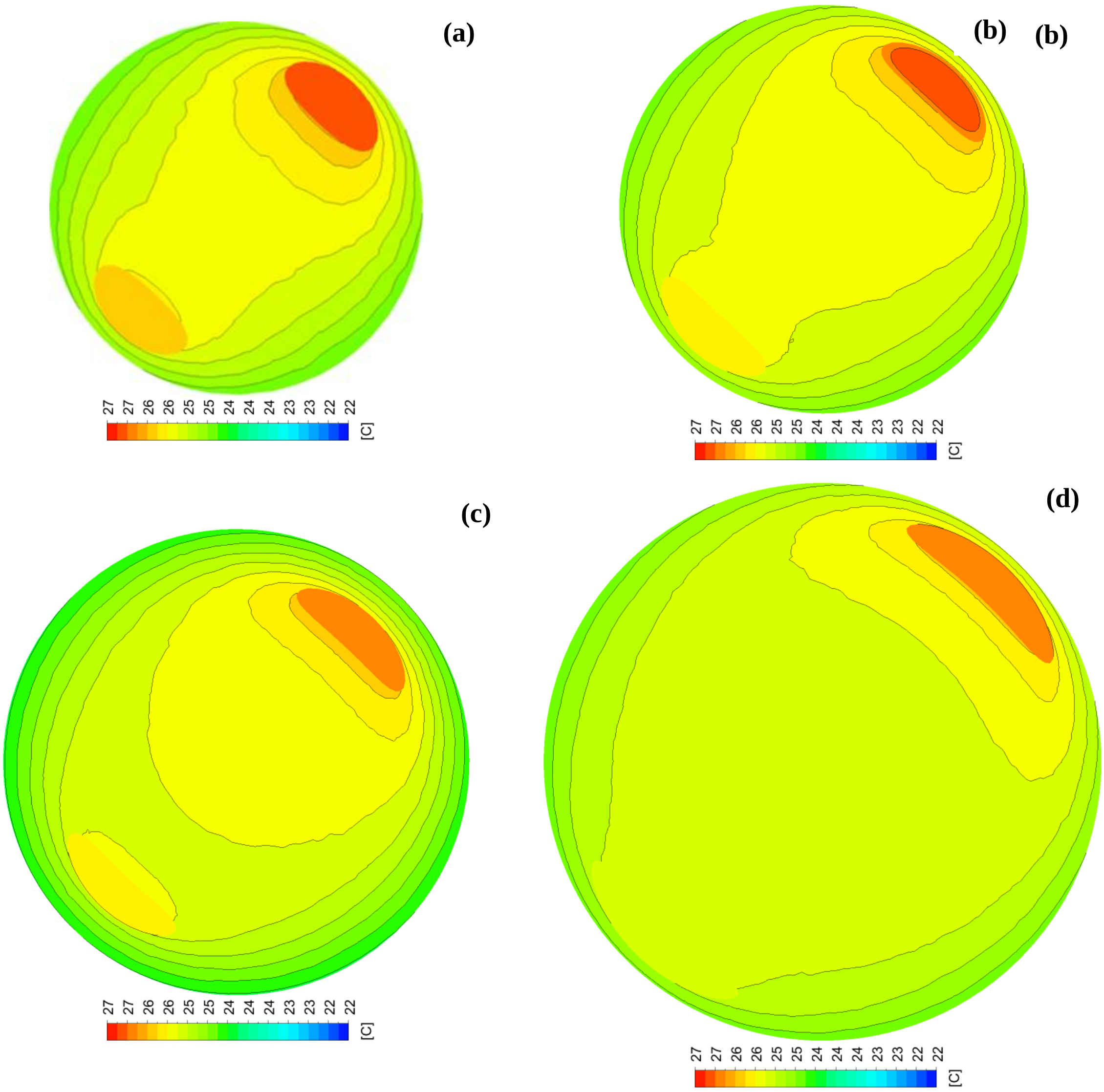

Fig. 29. Temperature contours on a horizontal plane at a depth of 10 m at different borehole diameters: (a) 180, (b) 240, (c) 300, and (d) 360 mm

6.4. Response surface

The response surface shown in **Fig. 30** illustrates the change in the output as a function of the inputs. In this study, two output variables were utilized: *COP* improvement and net thermal energy. In addition, it provides the approximated value of the output parameters quickly throughout the design space. Figure 31a, c, and e show the response surface of the *COP*, while **Fig. 30b, d, and f** show the response surface of Q_{net}. **Figures 30a–d** are drawn in the surface plot as the input parameters' span is continuous, while **Figs 30e and f** are shown in vertical bar charts, where the input variables are considered discrete. These figures demonstrate that the spiral radius and grout conductivity have a linear impact on both outputs. Increasing both parameters increases these outputs, indicating that the heat transfer is enhanced significantly compared to the pressure drop and pumping power increment.

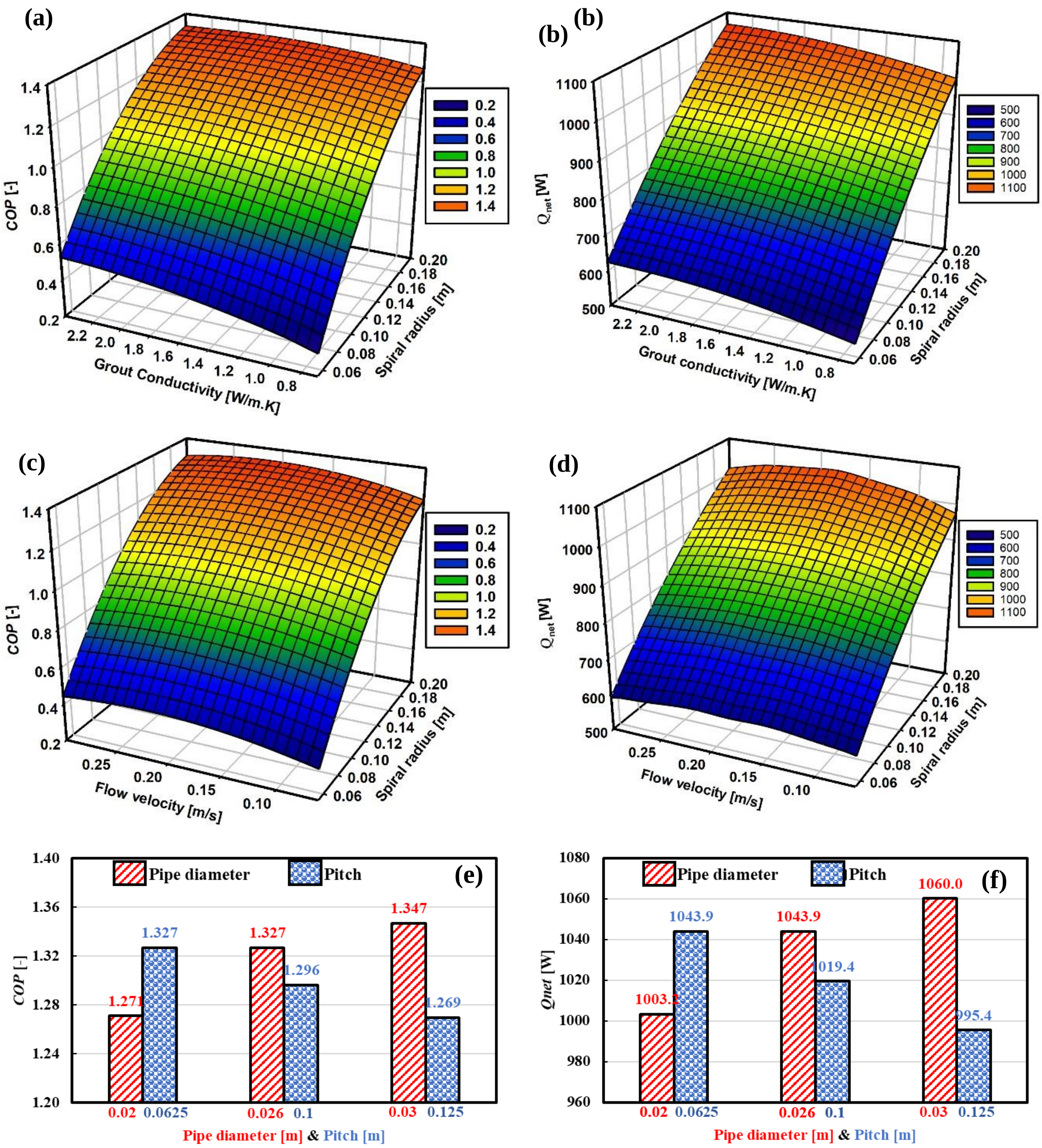

Fig. 30. Surface response of each output (a, c, and d) *COP*_improvement and (b, d, and f) Q_{net}

Fluid velocity has a polynomial relationship with the *COP* and Q_{net}. Both outputs increase with the increment of the fluid velocity to the critical value of 0.21 m/s, and both outputs decrease gradually, as shown in **Fig 30 c and d.** Increasing the fluid velocity more than 0.21 m/s will result in more pressure drop and pumping pump than the enhancement in the heat gain.

Concurrently, the pipe diameter and pitch distance have a contradictory impact on both outcomes. Doubling the pitch distance decreased the *COP* and Qnet by 8.0 % and 4.4 %, while increasing the pipe diameter from 0.2 m to 0.03 m increased *COP* and Qnet by 11.4 % and 5.5 %, respectively.

6.5. Sensitivity analysis

The local sensitivity analysis chart allows the change of the outputs based on the inputs' change independently at a specific response point, as shown in **Fig. 31a**. The spiral radius has a significant impact on Q_{net} and *COP*, while the flow velocity affects thermal effectiveness, followed by the pipe diameter. In contrast, the other variables have an irrelevant influence, as demonstrated by the global sensitivity chart shown in **Fig. 31b.** The global sensitivity analysis considers all possible values for the input parameters other than the local sensitivity analysis, which depends on the local parameter values.

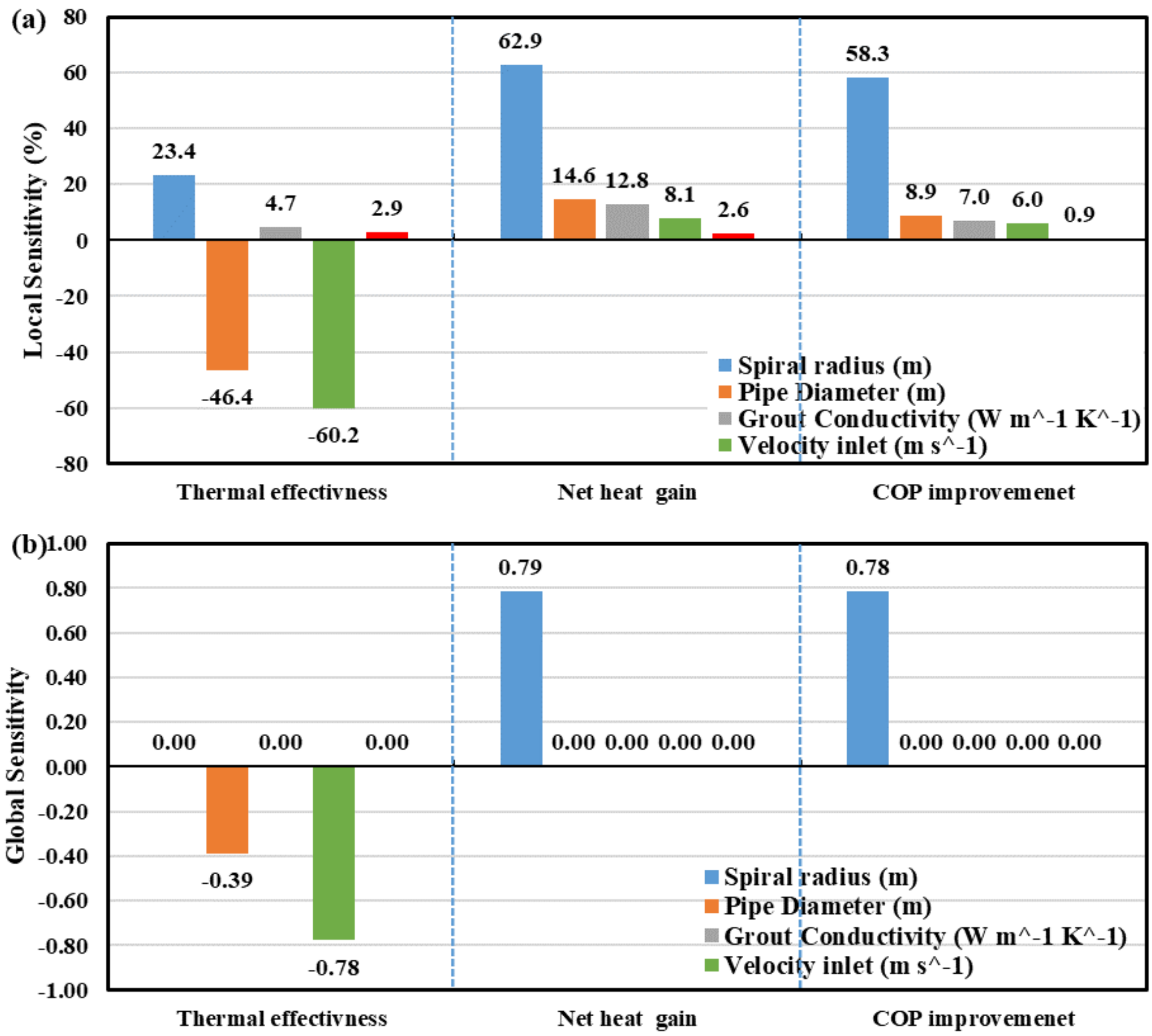

Fig. 31. a) Local and b) global sensitivity analyses

6.6. Optimization

The MOGA algorithm was applied to optimize the design and operating variables, thus fulfilling the defined objective functions. The objectives were to maximize both the *COP* and Qnet. The MOGA algorithm selected three optimum candidates from a new sample set, as shown in **Fig. 32.**

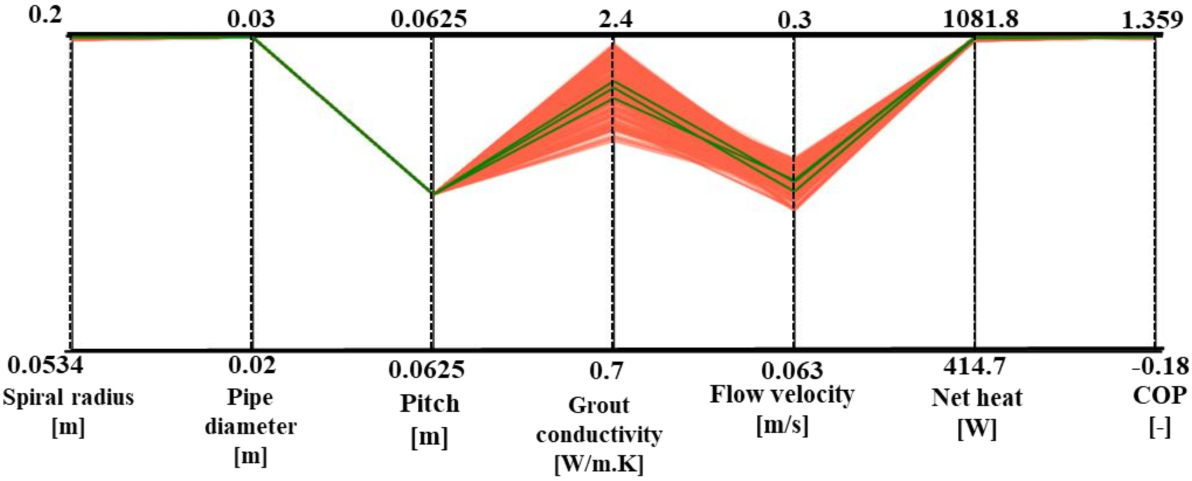

Fig. 32. Sample chart is generated by MOGA algorithm

The trade-off charts for each variable are shown in **Fig. 33,** which illustrates the effect on outputs when input variables are changed. This chart type is a powerful tool for identifying optimum decisions.

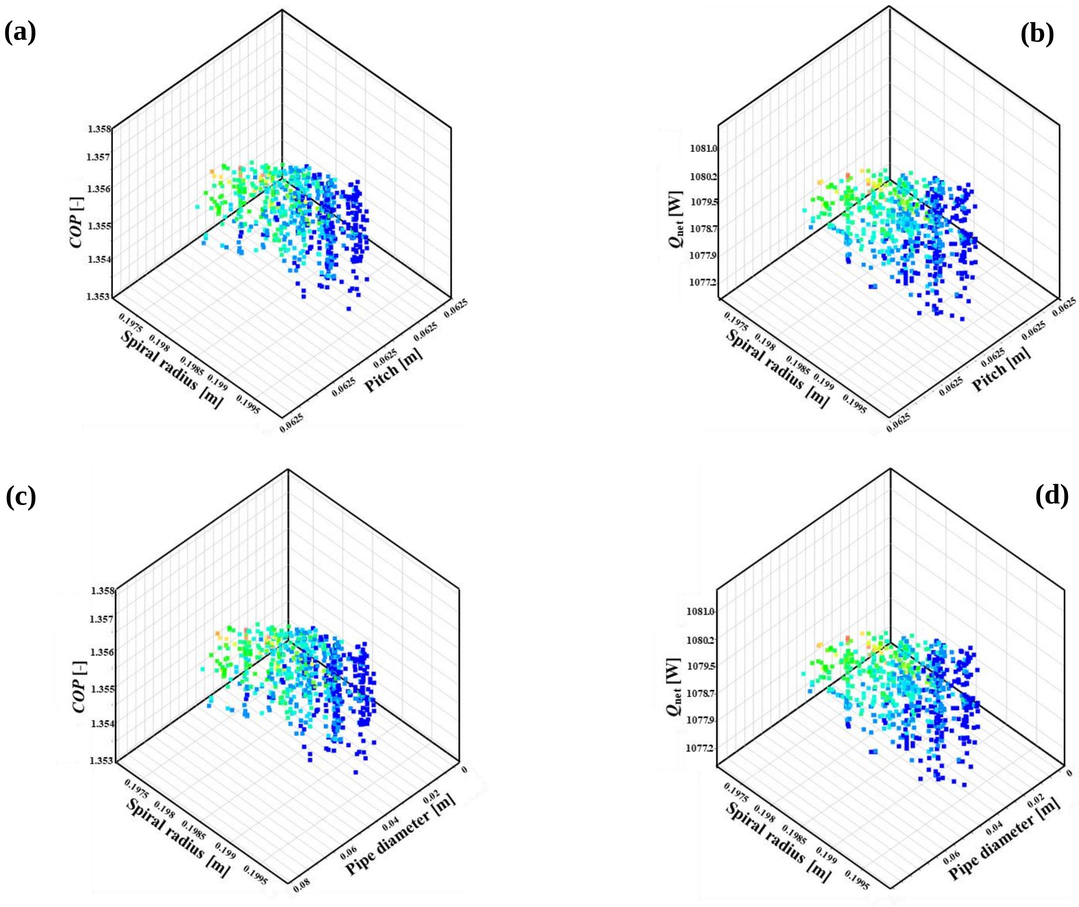

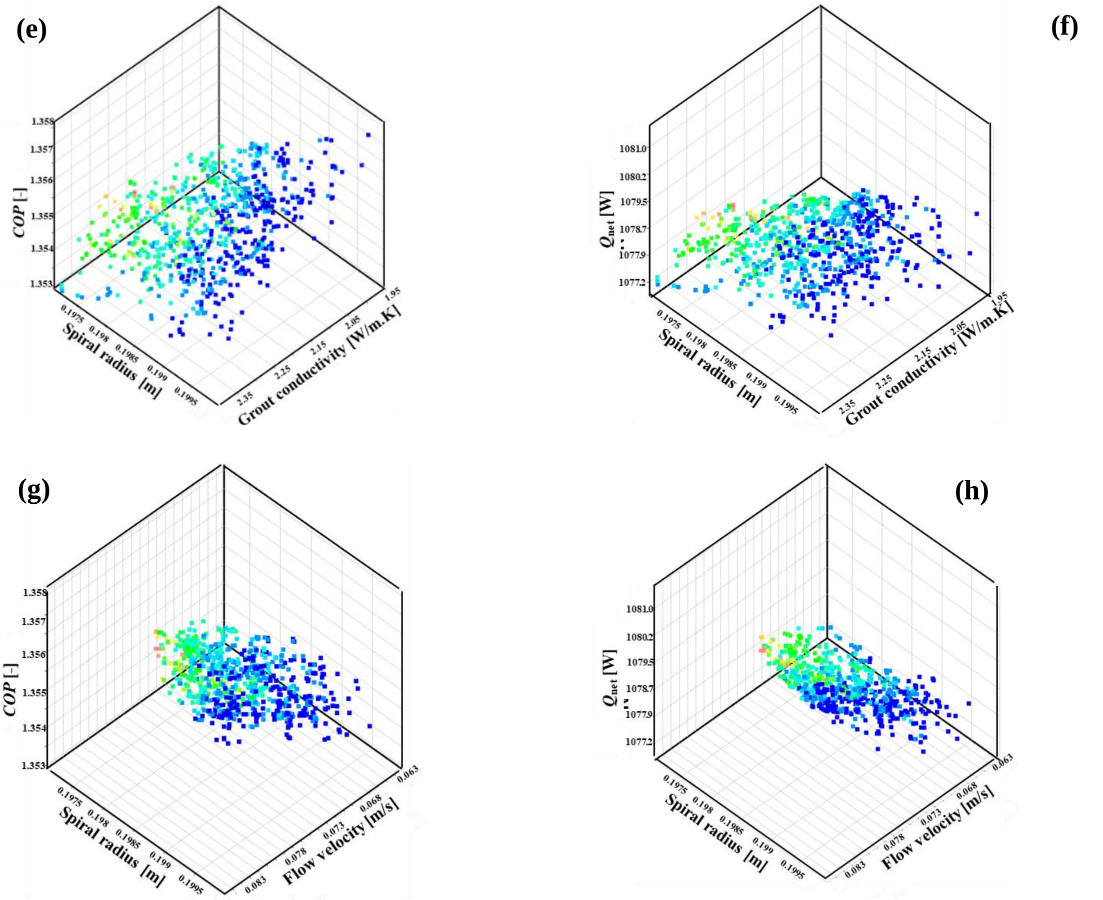

Fig. 33. Trade-off charts for each parameter on each output (a, c, e, and g) *COP* and (b, d, f, and h) Q_{net}. The blue color indicates a possible feasible value

The correlation matrix shown in **Fig. 34** illustrates key parameters and correlations between all parameters. It is evident that grout conductivity has a weak correlation with pipe diameter and pitch distance. While the outputs of *COP* and Qnet are strongly correlated with the spiral radius, the grout conductivity and other parameters are insignificantly correlated. In addition, the effectiveness depends mainly on the flow velocity, followed by pipe diameter.

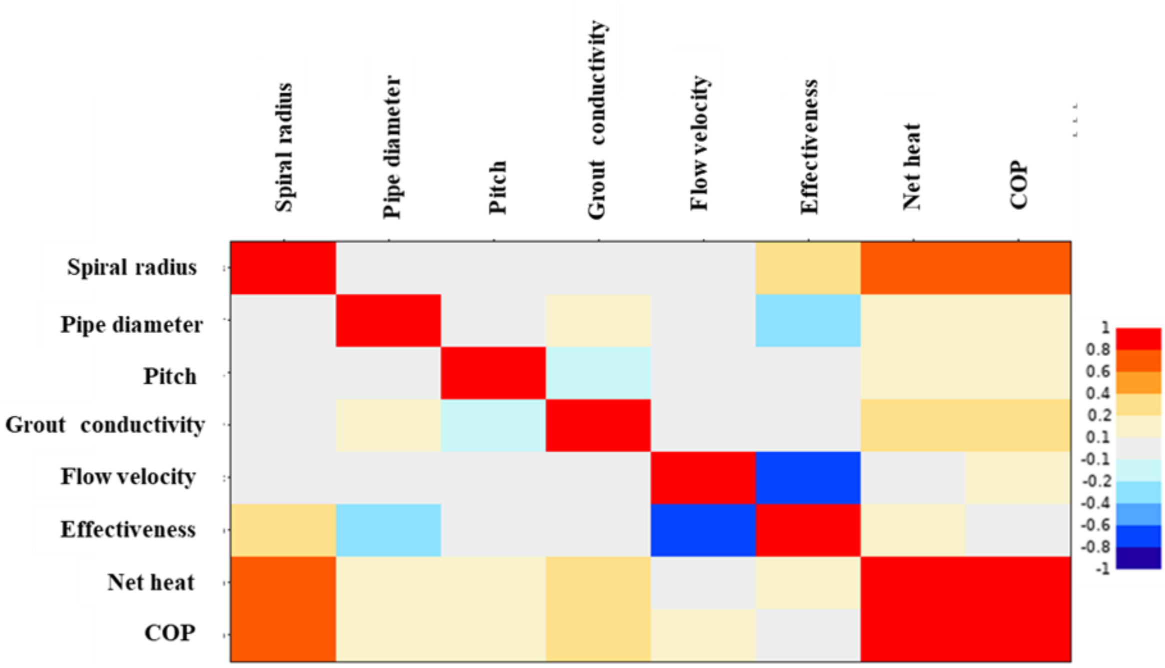

Fig. 34. Correlation matrix

Finally, Table 6 lists the three optimum candidates that satisfy the optimization criterion.

Table 6 Optimum candidates

	Candidate #1	Candidate #2	Candidate #3
Spiral radius [m]	0.2	0.2	0.2
Pipe diameter [m]	0.03	0.03	0.03
Pitch [m]	0.0625	0.0625	0.0625
Grout conductivity [W/m.K]	2.16	2.12	2.07
Flow velocity [m/s]	0.19	0.18	0.19
Net heat [W]	1080	1079.5	1078.6
COP [-]	1.356	1.357	1.358

7. Conclusions

The present study numerical investigated the performance of a novel spiral-double GHX as an alternative to the conventional U-tube and spiral GHX. The new GHX decreased the construction cost and facilitated the installation process. The numerical results results are concluded as follows:

- The spiral-double GHX achieved better thermal effectiveness (*E*) for all flow rates, with an average increment of 40.8 %, compared with the single U-tube GHX.
- The spiral-double GHX rejects more thermal energy, with an average increment of 44.1 %, compared with the single-U-tube GHX.

- The thermal resistance (R_b) of the spiral-double GHX is lower than that of the single-U tube GHX by 66.9 % and 75.3 % for 2 and 8 L/min flow rates.
- The *COP*_improvement is 0.4 and 0.5 for laminar and turbulent flow conditions compared with 0.26 and 0.36 for spiral GHX.
- The sensitivity analysis shows that the spiral radius has a significant impact on Q_{net} and *COP*, while the flow velocity affects the thermal effectiveness, followed by the pipe diameter.
- Finally, the optimization indicates that the critical fluid velocity is 0.21 m/s with an optimum pipe diameter of 0.03 m, pitch of 0.0625 m, a spiral radius of 0.2, and grout conductivity of 2.1 W/m.K.

Consequently, this advantage could improve the performance of the GSHP used for cooling and heating of the building and decreasing the number of boreholes required to carry the building heating and cooling loads.

The future work focusing on the long-term thermal performance analysis of the whole GSHP system, long-term analysis is a must to evaluate the degradation in the system performance as well as the energy savings and the economic feasibility of using the new spiral-double GHX.

Acknowledgment

This work is a part of the NEDO project for developing a new thermal application. The authors would like to acknowledge the New Energy and Industrial Technology Development Organization (NEDO) for funding this research. Also, The authors would like to acknowledge Mr. Oe Motoaki from INOAC HOUSING & CONSTRUCTION MATERIALS CO., LTD, JAPAN for providing the helical tubes.

References

[1] Liang B, Chen M, Fu B, Li H. Investigation on the thermal and flow performances of a vertical spiral-tube ground heat exchanger in sand combined with kaolin additive. Energy Build 2019;190:235–45. doi:https://doi.org/10.1016/j.enbuild.2019.03.003.

[2] Sáez Blázquez C, Borge-Diez D, Martín Nieto I, Farfán Martín A, González-Aguilera D. Technical optimization of the energy supply in geothermal heat pumps. Geothermics 2019;81:133–42. doi:https://doi.org/10.1016/j.geothermics.2019.04.008.

[3] Lamarche L. Horizontal ground heat exchangers modelling. Appl Therm Eng 2019;155:534–45. doi:https://doi.org/10.1016/j.applthermaleng.2019.04.006.

[4] Li C, Guan Y, Yang R, Lu X, Xiong W, Long A. Effect of inner pipe type on the heat transfer performance of deep-buried coaxial double-pipe heat exchangers. Renew

Energy 2020;145:1049–60. doi:https://doi.org/10.1016/j.renene.2019.06.101.

[5] Serageldin AA, Sakata Y, Katsura T, Nagano K. Thermo-hydraulic performance of the U-tube borehole heat exchanger with a novel oval cross-section: Numerical approach. Energy Convers Manag 2018;177:406–15. doi:10.1016/j.enconman.2018.09.081.

[6] Jalaluddin, Miyara A. Thermal performance and pressure drop of spiral-tube ground heat exchangers for ground-source heat pump. Appl Therm Eng 2015;90:630–7. doi:https://doi.org/10.1016/j.applthermaleng.2015.07.035.

[7] Hamada Y, Saitoh H, Nakamura M, Kubota H, Ochifuji K. Field performance of an energy pile system for space heating. Energy Build 2007;39:517–24. doi:https://doi.org/10.1016/j.enbuild.2006.09.006.

[8] Kayaci N, Demir H, Kanbur BB, Atayilmaz ŞO, Agra O, Acet RC, et al. Experimental and numerical investigation of ground heat exchangers in the building foundation. Energy Convers Manag 2019;188:162–76. doi:https://doi.org/10.1016/j.enconman.2019.03.032.

[9] Zhang W, Yang H, Lu L, Fang Z. Investigation on influential factors of engineering design of geothermal heat exchangers. Appl Therm Eng 2015;84:310–9. doi:https://doi.org/10.1016/j.applthermaleng.2015.03.023.

[10] Chen S, Mao J, Han X. Heat transfer analysis of a vertical ground heat exchanger using numerical simulation and multiple regression model. Energy Build 2016;129:81–91. doi:10.1016/j.enbuild.2016.07.010.

[11] Li Y, Mao J, Geng S, Han X, Zhang H. Evaluation of thermal short-circuiting and influence on thermal response test for borehole heat exchanger. Geothermics 2014;50:136–47. doi:10.1016/j.geothermics.2013.09.010.

[12] Baek SH, Yeo MS, Kim KW. Effects of the geothermal load on the ground temperature recovery in a ground heat exchanger. Energy Build 2017;136:63–72. doi:https://doi.org/10.1016/j.enbuild.2016.11.056.

[13] Acuña A, Lara F, Rosales P, Suastegui J, Velázquez N, Ruelas A. Impact of a vertical geothermal heat exchanger on the solar fraction of a solar cooling system. Int J Refrig 2017;76:63–72. doi:https://doi.org/10.1016/j.ijrefrig.2017.02.007.

[14] Qi D, Pu L, Ma Z, Xia L, Li Y. Effects of ground heat exchangers with different connection configurations on the heating performance of GSHP systems. Geothermics 2019;80:20–30. doi:https://doi.org/10.1016/j.geothermics.2019.02.002.

[15] Congedo PM, Lorusso C, Baglivo C, Milanese M, Raimondo L. Experimental validation of horizontal air-ground heat exchangers (HAGHE) for ventilation systems.

Geothermics 2019;80:78–85. doi:https://doi.org/10.1016/j.geothermics.2019.02.010.

[16] Warner J, Liu X, Shi L, Qu M, Zhang M. A novel shallow bore ground heat exchanger for ground source heat pump applications—Model development and validation. Appl Therm Eng 2020;164:114460. doi:https://doi.org/10.1016/j.applthermaleng.2019.114460.

[17] Zarrella A, De Carli M, Galgaro A. Thermal performance of two types of energy foundation pile: Helical pipe and triple U-tube. Appl Therm Eng 2013;61:301–10. doi:https://doi.org/10.1016/j.applthermaleng.2013.08.011.

[18] Sáez Blázquez C, Farfán Martín A, Martín Nieto I, Carrasco García P, Sánchez Pérez LS, González-Aguilera D. Efficiency analysis of the main components of a vertical closed-loop system in a borehole heat exchanger. Energies 2017;10:1–15. doi:10.3390/en10020201.

[19] Zarrella A, Capozza A, De Carli M. Analysis of short helical and double U-tube borehole heat exchangers: A simulation-based comparison. Appl Energy 2013;112:358–70. doi:10.1016/j.apenergy.2013.06.032.

[20] Saeidi R, Noorollahi Y, Esfahanian V. Numerical simulation of a novel spiral type ground heat exchanger for enhancing heat transfer performance of geothermal heat pump. Energy Convers Manag 2018;168:296–307. doi:10.1016/j.enconman.2018.05.015.

[21] Zhao Q, Chen B, Liu F. Study on the thermal performance of several types of energy pile ground heat exchangers: U-shaped, W-shaped and spiral-shaped. Energy Build 2016;133:335–44. doi:10.1016/j.enbuild.2016.09.055.

[22] Javadi H, Mousavi Ajarostaghi SS, Pourfallah M, Zaboli M. Performance analysis of helical ground heat exchangers with different configurations. Appl Therm Eng 2019;154:24–36. doi:10.1016/j.applthermaleng.2019.03.021.

[23] Javadi H, Ajarostaghi SSM, Mousavi SS, Pourfallah M. Thermal analysis of a triple helix ground heat exchanger using numerical simulation and multiple linear regression. Geothermics 2019;81:53–73. doi:10.1016/j.geothermics.2019.04.005.

[24] Javadi H, Mousavi Ajarostaghi SS, Rosen MA, Pourfallah M. Performance of ground heat exchangers: A comprehensive review of recent advances. Energy 2019;178:207–33. doi:https://doi.org/10.1016/j.energy.2019.04.094.

[25] Laloui L, Rotta Loria AF. Design of details for construction of energy geostructures. Anal Des Energy Geostructures 2020:1003–22. doi:10.1016/b978-0-12-816223-1.00016-3.

[26] TL J, Yeoh GH, Liu C. Computational Fluid Dynamics A Practical Approach. First edit. Elsevier Inc; 2013.

[27] ANSYS I. Computational fluid dynamics 2018. https://www.ansys.com/products/fluids.

[28] Song W, Zheng T, Liu X, Yang J, Zhang C. Data analysis and discussion of thermal response test under a power outage and variable heating power. Case Stud Therm Eng 2020;20. doi:10.1016/j.csite.2020.100632.

[29] Editor(s): Galen J. Suppes TSS. Production of Electricity. Sustain Nucl Power, Acad Press 2007:185–200. doi:10.1016/b978-012370602-7/50024-7.

[30] Dube Kerme E, Fung AS. Transient heat transfer simulation, analysis and thermal performance study of double U-tube borehole heat exchanger based on numerical heat transfer model. Appl Therm Eng 2020;173. doi:10.1016/j.applthermaleng.2020.115189.

[31] Zhang C, Xu H, Fan J, Sun P, Sun S, Kong X. The coupled two-step parameter estimation procedure for borehole thermal resistance in thermal response test. Renew Energy 2020;154:672–83. doi:10.1016/j.renene.2020.03.019.

[32] Javed S, Spitler JD. Calculation of borehole thermal resistance. Adv. Ground-Source Heat Pump Syst., vol. 1, Woodhead Publishing Limited; 2016, p. 63–95. doi:10.1016/B978-0-08-100311-4.00003-0.

[33] ANSYS I. Design Exploration User ' s Guide 2013;15317:724–46.

[34] Abdeen A, Serageldin AA, Ibrahim MGE, El-Zafarany A, Ookawara S, Murata R. Solar chimney optimization for enhancing thermal comfort in Egypt: An experimental and numerical study. Sol Energy 2019;180:524–36. doi:10.1016/j.solener.2019.01.063.

Appendix A

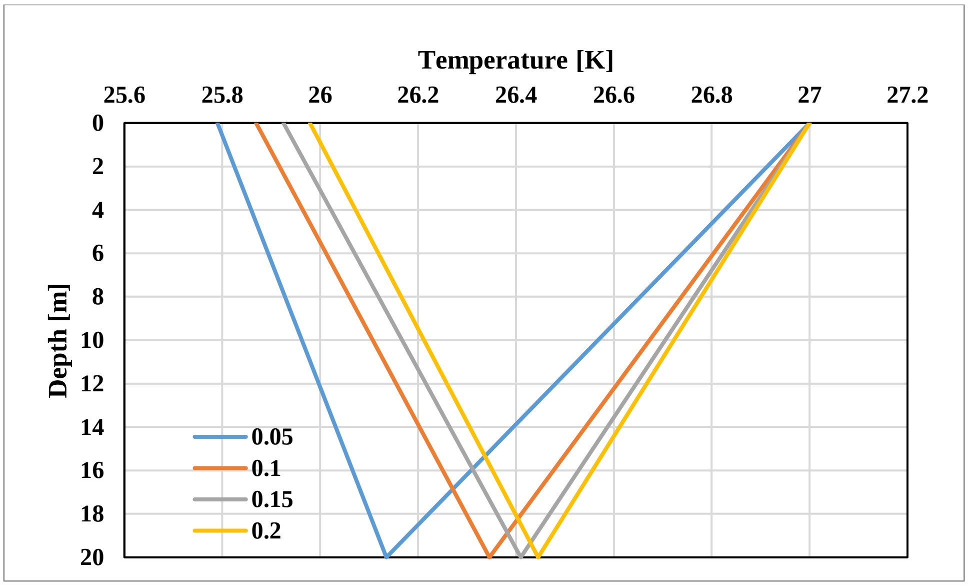

Fig. A1 Pitch impact on fluid temperature profile

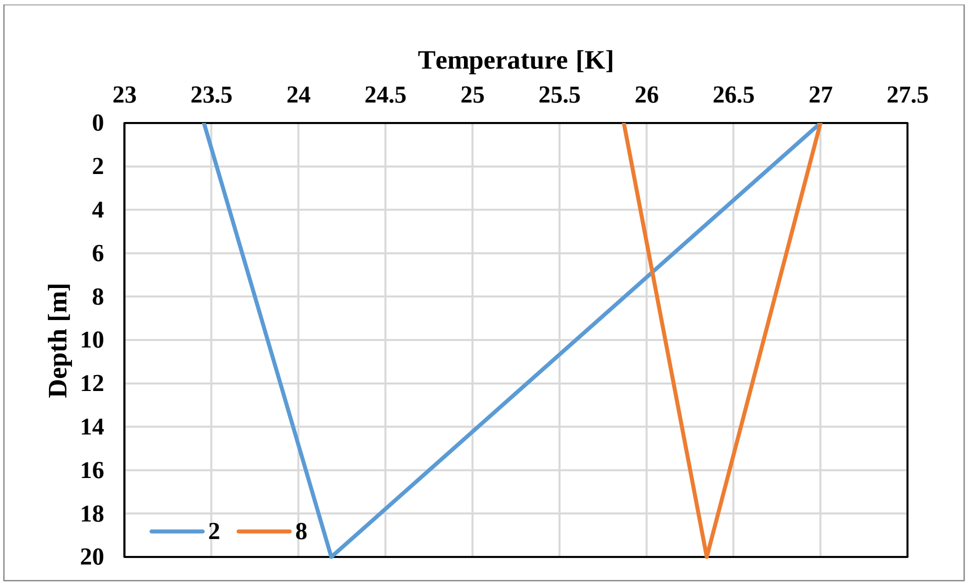

Fig. A2 Flow rate impact on fluid temperature profile

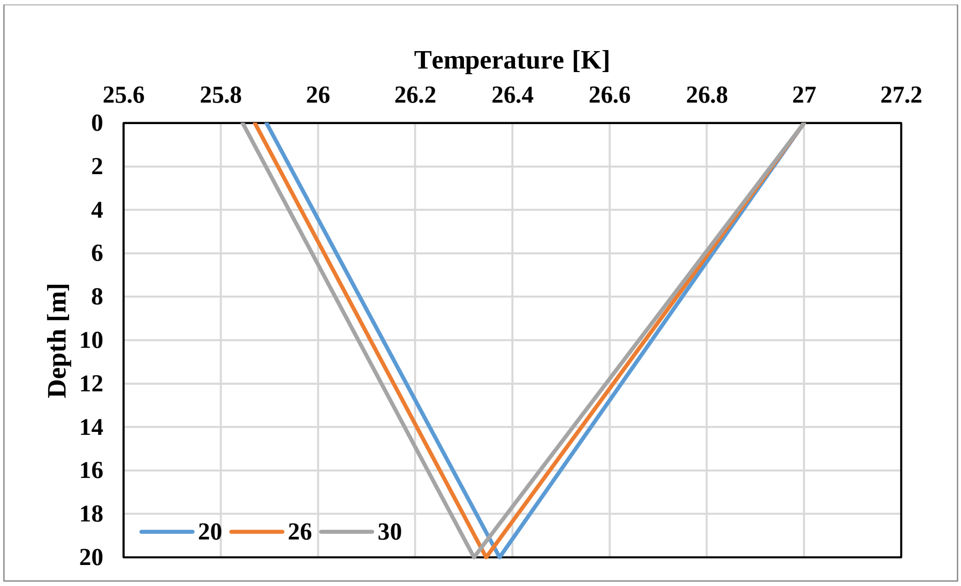

Fig. A3 Tube diameter impact on fluid temperature profile

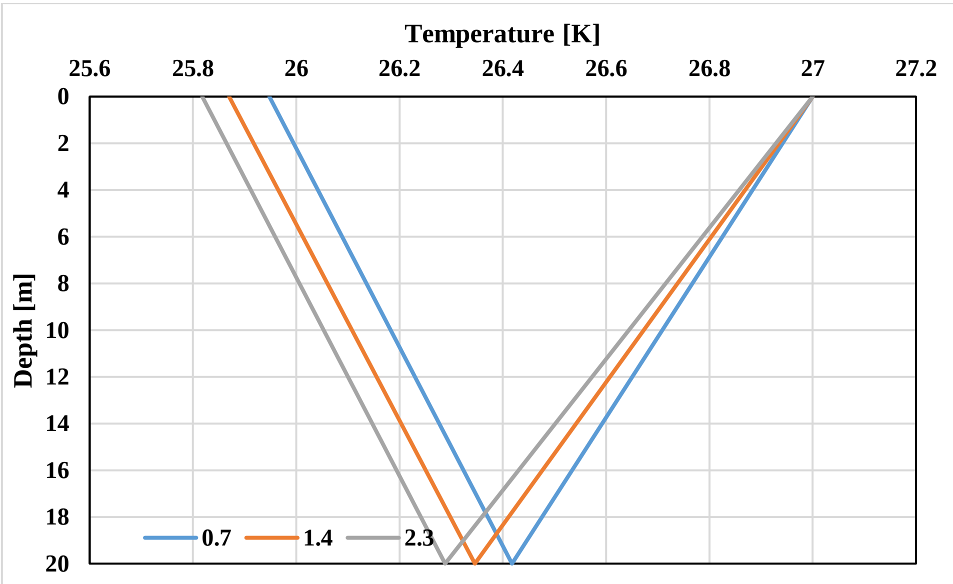

Fig. A4 Grout conductivity impact on fluid temperature profile

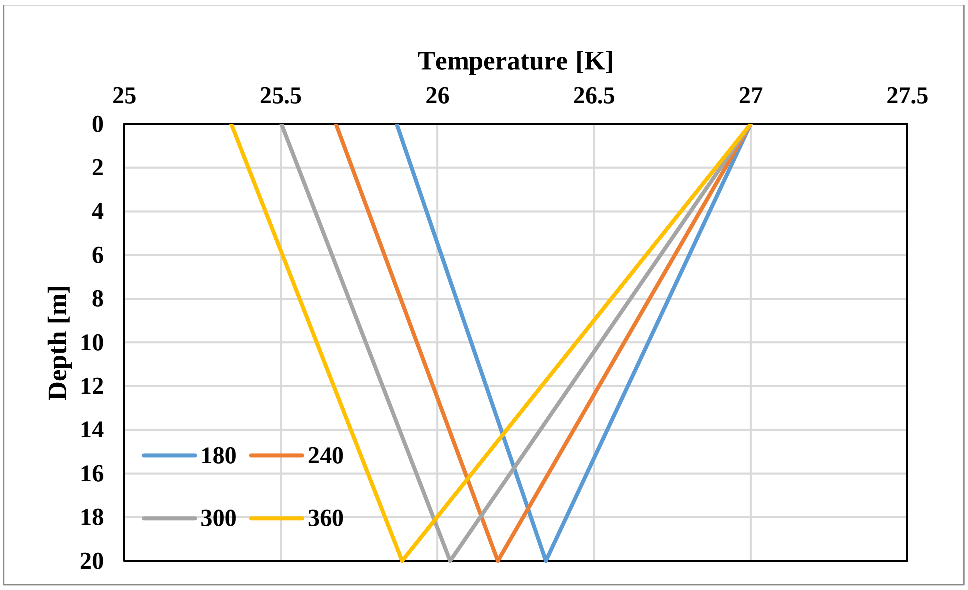

Fig. A5 Spiral radius impact on fluid temperature profile